Project Reference Number: ARCP2012-21NSY-Siswanto

Spatial and temporal variations of Biological Production in the Asia-Pacific Marginal Seas

The following collaborators worked on this project:

Eko Siswanto, Japan Agency for Marine-Earth Science and Technology, Japan, ekosiswanto@jamstec.go.jp

Anukul Buranapratheprat, Burapha University, Thailand, anukul@buu.ac.th

Joji Ishizaka, Nagoya University, Japan, jishizak@hyarc.nagoya-u.ac.jp

Tong Phuoc Hoang Son, Institute of Oceanography, Vietnam, tongphuochoangson@gmail.com

Katsuhisa Tanaka, Japan International Research Center for Agricultural Sciences, katuhi@affrc.go.jp

Spatial and temporal variations of Biological Production in the Asia-Pacific Marginal Seas

Project Reference Number: ARCP2012-21NSY-Siswanto
Final Report submitted to APN

PAGE LEFT INTENTIONALLY BLANK

OVERVIEW OF PROJECT WORK AND OUTCOMES

Minimum 2pages (maximum 4 pages)

Non-technical summary

This research project consists several main activities which are considered to be able to improve research capability in the Asia-Pacific region, especially in the collaborating countries. In terms of research, the project focused on discerning spatial and temporal variations of marine biological production in the Asia-Pacific marginal seas (the East China Sea, the South China Sea, the Strait of Malacca, and the Gulf of Thailand) utilizing multisensor satellite observations and coupled hydrodynamic-biogeochemical model. As part of the research achievements, one paper was accepted (in press) for publication in Remote Sensing. Other three or four papers are now under preparation for submission to high impact journals. To achieve research objectives, four (4) young scientists from collaborating countries were also involved in the project, that at once allowing them to improve their research capability and to enter international scientific community. In order to expand international networking and/or research collaboration in the near future, international mini-workshop on the western Pacific Ocean and marginal seas biogeochemical variability was also held in Japan Agency for Marine-Earth Science and Technology (JAMSTEC) in February 2014. As feedback of this research project and research continuation, it has been discussed and planned to propose Japan Society for the Promotion of Science (JSPS) Postdoctoral Fellowships for foreign researchers.

Keywords

Remote sensing, ocean color, phytoplankton, primary production, coastal upwelling, vertical mixing, atmospheric depositions, biogeochemical cycle, numerical/biogeochemical model, Asian monsoons, El Nino/La Nina, Indian Ocean Dipole

Objectives

The main objectives of the project were:

1. To discern spatial and temporal variations of phytoplankton biomass and primary production in the various marginal seas within the Asia-Pacific region applying multisensor satellite observations and coupled hydrodynamic-biogeochemical model;
2. To identify the most predominant factors/drivers and the probable mechanisms underlying the observed spatial and temporal variations of phytoplankton biomass and/or primary production;
3. To strengthen research capability and research collaboration in the Asia-Pacific region, especially among the research collaborating countries;
4. To educate and nurture young scientists, allowing them to improve their research capability by involving them in this research project.

Amount received and number years supported

The Grant awarded to this project was:
US$ 34,400 for Year 1 (received)
US$ < 8,600 for Year 2 (expected)

Activity undertaken

Activities which were undertaken within this research project were:

1. Research activities focused in the marginal seas of the East China Sea, the South China Sea, the Strait of Malacca, and the Gulf of Thailand;
2. Involving young scientists from the collaborating countries in the research project activities;
3. Holding international APN-JAMSTEC mini-workshop in JAMSTEC from 3 to 4 February 2014;
4. Publishing research finding in high impact scientific journal (in press in Remote Sensing).

Results

Achievements from this research project can be pointed out as follows;

1. In terms of research outcomes, research project provided a comprehensive understanding on the a meridional/region-specific differences in the phytoplankton biomass and/or primary production seasonal cycles, as well as the predominant drivers/mechanisms;
2. It is also understood that phytoplankton biomass and primary production in the marginal seas of the Asia-Pacific region are sensitive to large scale climatic anomalies both in the Pacific Ocean and Indian Ocean;
3. Still in terms of research, research project also found that in phytoplankton biomass and primary production in the Asia-Pacific marginal seas showed decadal trends;
4. Young scientists involved in this project are now able to improve their own research project, their research capability, not only to complete their university degree, but also for their future career;
5. International mini-workshop was successfully held in JAMSTEC, Yokohama, from 3 to 4 February 2014;
6. International networking, for the future research collaboration in the Asia-Pacific region, can be expanded not only among the scientists in the collaborating countries, but also other non-member Asia-Pacific countries participating in the mini-workshop;
7. Several publications are expected to be publishable in the high impact journal, one of them was already accepted (in press) for publication in Remote Sensing high impact journal;
8. Agreements to propose JSPS Postdoctoral Fellowships for researchers from Vietnam, Thailand, China, with P.I. of this project as host researcher.

Relevance to the APN Goals, Science Agenda and to Policy Processes

Because this research project is a regional research collaboration among the four countries, Malaysia, Thailand, Vietnam, and Japan, it has strengthened interactions among scientists and improved research capability of the scientist in this region, hence improved scientific understanding on the specific area of change in marine domain related to climatic change and human activities. Based on the outputs of the project and through regional collaboration, recommendations for the future marine environment sustainability in the Asia-Pacific region can be provided as input to policy decision-making. In the near future (May 2014), scientists participated in the last APN-JAMSTEC international mini-workshop and scientists from WESTPAC forum will be invited to join Global Earth Observation System of Systems (GEOSS) symposium to discuss and develop mechanism meta-data exchange, one of the issues highlighted during the mini-workshop.

Self evaluation

Considering the following facts of; 1) the project gained fruitful scientific/research outcomes; 2) the project successfully achieved research objectives; 3) the project is able to educate/nurture young scientists to improve their research capability; 4) the project is able to organize international workshop for the future/further research collaborations; 5) the project is able to publish its scientific findings in the high impact scientific journal, with more papers are now under preparation; 6) agreements to do future research collaborations under the Japan Society for the Promotion of Science (JSPS) Postdoctoral Fellowships for foreign researchers, our self-evaluation for this research project is excellent

Potential for further work

There are several works that are potent to be carried in the near future, probably under the JSPS Postdoctoral Fellowships, such as; 1) assimilating satellite observation and biogeochemical model to study phytoplankton biomass and primary production variations in the South China Sea with longer time scale, i.e., to past decade reconstruction and future decade forecasting; 2) developing local primary production model specific for the South China Sea; 3) developing local phytoplankton biomass algorithms for the Strait of Malacca and the East China Sea to be used with MODIS ocean color sensors.

Publications (please write the complete citation)

Siswanto, E.; Tanaka, K. Phytoplankton Biomass Dynamics in the Strait of Malacca within the Period of the SeaWiFS Full Mission: Seasonal Cycles, Interannual Variations, and Decadal-scale Trends. Remote Sensing, 2014 (in press).

Acknowledgments

This research project was supported by a grant from the Asia-Pacific Network for Global Change Research (APN, ARCP2012-21NSY-Siswanto). We acknowledge Universiti Teknologi Malaysia, Burapha University, Japan International Research Centre for Agricultural Sciences, Nagoya University, and Nha Trang Institute of Oceanography for their institutional supports which led to smooth research activities. We thank all young scientists for their active involvement in this research project. Special thanks to all speakers who delivering their interesting talk and for their fruitful discussion during the APN-JAMSTEC international mini-workshop. We are grateful to reviewers whose constructive and valuable comments led to a greatly improved this research project proposal during the proposal preparation. Last but not least, we thank data providers, the Ocean Biology Processing Group (Code 614.2) at the GSFC, Greenbelt, Maryland, USA, for the production and distribution of the ocean color data, the Remote Sensing Systems and Physical Oceanography-Distributed Active Archive Center (PO.DAAC), Jet Propulsion Laboratory, for processing and distributing sea surface temperature and microwave-sensor-retrieved satellite data, respectively.

TECHNICAL REPORT

Minimum 15-20 pages (excluding appendix)

Preface

This document details the studies conducted in the Asia-Pacific marginal seas of the East China Sea, the South China Sea, the Gulf of Thailand, and the Strait of Malacca. Satellite observations and coupled hydrodynamic-biogeochemical model were applied to discern predominant factors/mechanisms underlying the observed phytoplankton biomass and primary production spatio-temporal variations. Depend upon the geographic positions of the marginal seas, there existed different seasonal cycle of phytoplankton biomass, responsivity of phytoplankton biomass on large/basin scale climatic anomalies, and phytoplankton biomass decadal trends. The predominant factors/mechanisms for phytoplankton variability will be comprehensively discussed in this document.

Table of Contents

1. Introduction

A marginal sea is a partially enclosed sea adjacent to or widely open to the open ocean at the surface, but bounded by submarine ridges on the sea floor. Despite remarkably narrower area compared to global open oceans, the world's marginal seas have marine phytoplankton biological production comparable to global ocean's production. Commercial fisheries in the marginal seas depend largely on the primary production of phytoplankton (Ryther, 1969; Iverson, 1990), as fish feed directly on phytoplankton, which are the base of the marine food web. Phytoplankton also play an important role in marine biogeochemical cycles. Through photosynthesis, marine phytoplankton assimilate inorganic carbon and thereby serve as a sink for atmospheric carbon dioxide. Chlorophyll-a (hereafter Chl-a) is commonly used as a metric of phytoplankton biomass for the purposes of estimating primary production (PP) from satellite observations. All phytoplankton contain Chl-a, or in

the case of Prochlorococcus sp., divinyl Chl-a (Huot et al., 2007). Chl-a, however, is subject to spatial and temporal variations, and such variations affect phytoplankton-dependent marine carbon dynamics and higher trophic level marine organisms.

Marginal seas in the Asia-Pacific region consist of the Japan/East Sea, the East China Sea (ECS), the South China Sea (SCS), and the connected semi-enclosed waters of the Strait of Malacca (SM), the Gulf of Thailand (GoT), and the Sulu Sea. Among those marine environments, the ECS, the SCS, the SM, and the GoT are considered to be vulnerable to both basin/large scale climatic anomalies and anthropogenic activities. This is due to their geographic locations which are between Indian and Pacific Oceans and surrounded by developing countries whose total population comprise more than half of the world's population and with the most-rapid population and economic growths.

The marine environment of the Asia-Pacific marginal sea is strongly influenced by the Asian monsoon (e.g., Wirtky, 1961; Tang et al., 2003; Gong et al., 2003; Tan et al., 2006; Siswanto et al., 2014). The Asian monsoon is characterized by annual reversing winds: dry southwesterly winds during the southwest monsoon (SWM, May–August) and wet northeasterly winds during the northeast monsoon (NEM, November–February) (e.g., Wirtky, 1961). In addition to the seasonal monsoon winds, the geographic position of the Asia-Pacific marginal seas, which is between the Indian and Pacific Oceans, makes the marine environment of the marginal seas subject to the influence of large-scale climatic anomalies such as the Indian Ocean Dipole (IOD) and El Niño/Southern Oscillation (ENSO). It is well known that, besides changes in precipitation associated with variations of the tradewinds to the west and east of the Indonesian archipelago, positive IOD and El Niño events both bring severe drought to Indonesia and Malaysia, and those droughts are very frequently followed by forest wildfires (Wang, et al., 2004; Yamagata, et al., 2013). Forest fires can be an important sources of macro- and micro-nutrients for phytoplankton growth as a result of atmospheric deposition of ash and aerosols (e.g., Abram et al., 2003). In this way coupled interactions between the atmosphere and ocean may provide a mechanism by which both the IOD and ENSO influence Chl-a and PP in the marginal seas. In addition to aforementioned natural factors, human activities, such as land clearing, mangrove deforestation, dam construction, fertilizer use, and the impacts of rapid population and economic growth along the coastal areas of the surrounding countries (Indonesia, Malaysia, Thailand, Vietnam, China, Korea, and Japan), also contribute to environmental changes in the marginal seas (Chua et al., 1998; Gong et al., 2006; Siswanto et al., 2008).

The aforementioned anthropogenic and natural perturbations are expected to cause spatial and temporal variations of oceanographic conditions, including Chl-a concentrations and hence PP in the marginal seas. While seasonal variation of Chl-a in the Asia-Pacific marginal seas have been reported previously (e.g., Tang et al., 2003; Gong et al., 2003; Tan et al., 2006; Siswanto et al., 2014), less are documented regarding the Chl-a interannual variation and long-term trend, as well as the probable predominant drivers, which may be associated with large scale climatic changes and long-term anthropogenic perturbations. Because of only low spatial resolution can be resolved by ship-borne and/or buoy-based observations (though may have high temporal resolution), the only feasible research approach to fully discern spatial and temporal marine biological production variation, as well as the probable drivers for the observed variations, is by utilizing multisensory satellite observations and numerical modeling. Therefore, research project consists of research activities that rely on multisensory satellite observation and that rely on the numerical modeling. The results and discussion of this document will be hence divided into two main topics, i.e., applications of satellite observation and numerical molding.

The goals of this research project carried out relying on the satellite observation are to (1) discern trends during the last decade, as well as spatial and temporal variations on seasonal and interannual time scales of satellite Chl-a and/or PP and (2) identify the mechanisms and predominant factors driving the trend during the last decade, as well as seasonal and interannual variations of observed Chl-a and/or PP. Depend upon the marginal seas, variability of in situ river discharge and re-analyzed surface salinity were also utilized. The topics off the researches emphasized for different marginal seas of the ECS, the SCS, and the SM are also different (see the following sections below).

While application of satellite observations were used for researches in the ECS, the SCS, and the SM, numerical/biogeochemical modeling was conducted for the SCS and GoT. Lower trophic-level ecosystem modeling is an attempt to simulate Chl-a dynamics by using computer techniques. Based on the conservation of mass, physical processes such as dilution, advection and diffusion that influence the concentration of a conservative substance. In addition to physical processes, however, Chl-a will be modified by biological and/or chemical processes. Chl-a might increase into the water column due to growth and reproduction and decrease due to mortality and being grazed by zooplankton while displacement is occurring. The processes are also dependent on environmental conditions and other living species in the ecosystem. Like research activities utilizing satellite observations, the goal of this numerical analysis is to investigate the relationship between Chl-a distributions and environmental conditions. Coupled with Princeton Ocean Model (POM), the ecosystem model is used to simulate Chl-a distributions in the SCS during the NEM (January) and the SWM (July).

In addition to modeling the SCS circulation, the influence of the SCS on the GoT water column and oceanographic conditions will also be reported in this document. Water column conditions in terms of vertical mixing and stratification are important to marine ecosystems and environments. In coastal seas, generally vertical well mixing is dominant due to tidal mixing and wind stirring. Some areas, however, where heat fluxes and freshwater fluxes from river discharge or atmospheric exchanges are very large, water column stratification is able to occur (Buranapratheprat et al., 2008a). The conditions of water column are crucial to physical and biochemical environments such as vertical material exchanges and PP of phytoplankton. Water stratification plays as a barrier to nutrient mixing between surface and subsurface waters, resulting in limited nutrient availability and low PP. In contrast, the stratification in a high eutrophic area can generate hypoxia in near bottom water due to organic material decomposition (Zhang et al., 2010). This occurs because dissolved oxygen (DO) is continually consumed while subsurface water is unable to exchange gases with air. Severity of the problem depends on amount of organic material, strength and duration of water column stratification.

2. Methodology

2.1. Application of Satellite Observations to Study Spatial and Temporal Chl-a variations

2.1.1. Study Regions and Research Targets

Depend upon the countries of research collaborators and data availability, research project focused on four main marginal seas i.e., the ECS, the SCS, the GoT, and the SM. Research in the ECS was focused on the interannual variation and trend of PP with special emphasis to discern the possible impact of the world's largest Three-Gorges Dam construction. One of researches conducted in the SCS was on the impacts of large scale climatic anomalies on the spatial and temporal variations of Chl-a. Other research was on the modelling the SCS water circulation and Chl-a applying coupled hydrodynamic-biogeochemical model. Connected to research of the SCS's water mass circulation, research on the influence of the SCS water mass on the water column of the GoT was also carried out. In the marginal sea of the SM, research was focused on the Chl-a seasonal cycle, interannual variation, and decadal trend. The study regions covered by this research project is illustrated in Figure 1.

In general, the target of the research is to discern the probable environmental variables (both oceanic and atmospheric) that drive the observed spatial and temporal variations of Chl-a and/or PP in the aforementioned Asia-Pacific marginal seas. As described in the proposal in the beginning of the project, satellite observations that will be detailed below are the main research tool/approach, beside other approach of in situ data and modelling were also used.

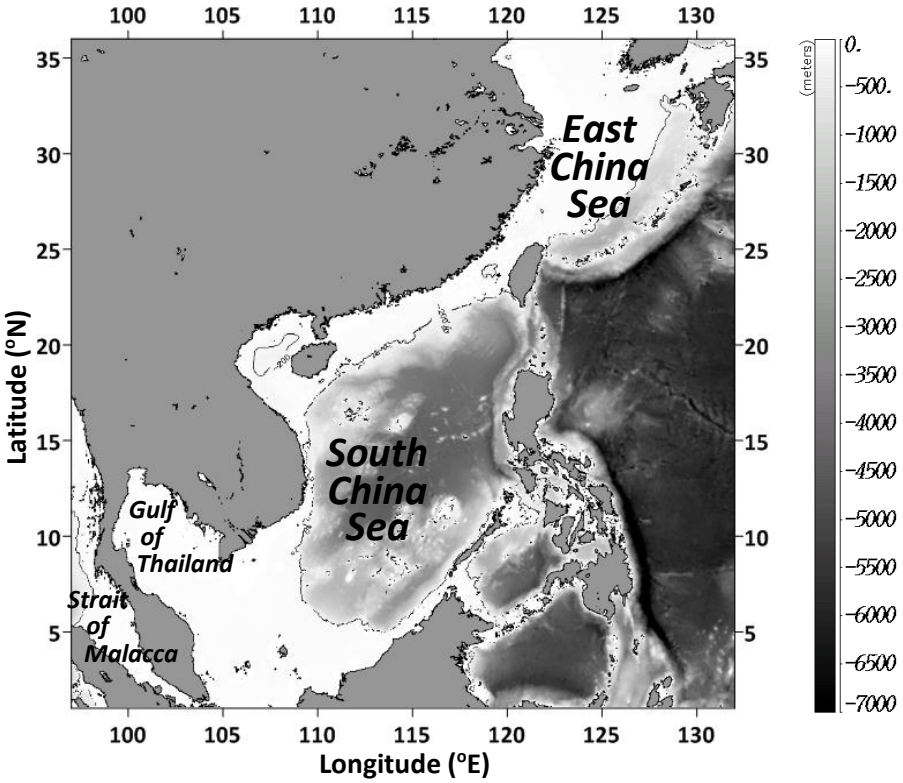

Figure 1. Bathymetry map showing the Asia-Pacific marginal seas of the ECS, the SCS, the GoT, and the SM. The black contour denotes the -200 m isobath.

2.1.2. Multisensor Satellite, In Situ, and Re-analyzed-Data Acquisitions

Data of Chl-a and aerosol optical thickness at 865 nm (AOT) derived from monthly SeaWiFS Level-3 (with 9-km spatial resolution) ocean color sensor during the full 13-year SeaWiFS mission were used in this study and acquired from the NASA *Ocean Biology* Processing *Group* (OBPG, http://oceancolor.gsfc.nasa.gov). The latest version of SeaWiFS Chl-a (SeaWiFS Reprocessing 2010.0, http://oceancolor.gsfc.nasa.gov/WIKI/OCReproc20100SW.html) was used to ensure the best quality of the Chl-a data. For the regions of the SCS and the SM, the SeaWiFS Chl-a data used here were processed using the standard black pixel assumption atmospheric correction (Gordon and Wang, 1994) and retrieved by using the NASA standard OC4v4 empirical Chl-a algorithm (O'Reilly et al., 1998). We masked all pixels with negative values of remote sensing reflectance at 412 nm. We considered the data from these pixels to be invalid because of an atmospheric correction failure.

Specifically for the ECS however, rather than using monthly Level-3 NASA standard Chl-a product, we used more reliable Chl-a data employing SeaWiFS level-2 (4-km spatial resolution) remote sensing reflectance (Rrs, from http://oceancolor.gsfc.nasa.gov) and applying local Chl-a algorithm (Siswanto et al., 2011). New product of Chl-a for the ECS was prepared by Hydrospheric Atmospheric Research Center (HyARC) of Nagoya University. Instead of Chl-a, PP spatial and temporal variations were more emphasized here to be compared with previously published papers of PP using in situ observation and model estimation (e.g., Gong et al., 2006; Liu et al., 2010). PP was estimated by also employing local algorithm specifically for the ECS proposed by Gong and Liu (2003) with the input variables of SeaWiFS Chl-a, attenuation coefficient (Kd), and photosynthetically available radiation (PAR).

Monthly sea surface temperature (SST) with 4-km spatial resolution retrieved by the Advanced Very High Resolution Radiometer (AVHRR, http://podaac.jpl.nasa.gov) from September 1997 to December 2009, and by the Moderate Resolution Imaging Spectroradiometer-Aqua (MODIS, http://oceancolor.gsfc.nasa.gov) from January 2010 to December 2010 were used to generate a SST dataset compatible with the 13-year SeaWiFS data. Other satellite data used in this study were wind

speed (WS) and rain rate (RR), which were retrieved by microwave sensors on the QuikScat satellite (from September 1997 to November 2009, acquired from http://www.ssmi.com) and the Tropical Rainfall Measuring Mission (TRMM) satellite Precipitation Radar (from September 1997 to December 2010, acquired from http://apdrc.soest.hawaii.edu), respectively. The spatial resolution of both the monthly WS and RR data was 0.25°. Satellite-derived SST, WS, and RR images were re-gridded to match the SeaWiFS Chl-a and AOT image dimensions.

As an attempt to understand the impacts of human activities from the land on marine biological production, we utilized river discharge (RD). To discern the influence of RD on the seasonal SeaWiFS-derived Chl-a variation in the SM, we acquired monthly climatological RD data archived by the Center for Sustainability and the Global Environment (SAGE, http://www.sage.wisc.edu/riverdata) for the four main rivers (Selangor, Perak, Klang, and Langat) that empty into the SM. On the other hand, to discern the impact of the Three-Gorges Dam (TGD) construction on the PP spatial and temporal variations monthly RD data derived from http://61.191.22.157/TYFW/InfoQuery/HeDaosec.aspx were prepared by HyARC of Nagoya University. In addition, FRA-JCOPE2 reanalyzed sea surface salinity (SSS) data generated by the Japan Agency for Marine-Earth Science (JAMSTEC, http://www.jamstec.go.jp/frcgc/jcope/htdocs/e/distribution/index.html) were utilized to delineate the low surface salinity Changjiang-diluted water (CDW) within which spatial and temporal variations of PP are largely influenced by Changjiang discharge. The CDW is defined the marine environment in the ECS characterized by low SSS of < 32 PSU (e.g., Siswanto et al., 2008). PP in the areas adjacent to Changjiang estuary is also largely controlled by total suspended sediment (TSM) (e.g., Gong et al., 2003; Siswanto et al., 2011). Therefore, as one possible explanatory variable for PP variation in the ECS, we estimated TSM from SeaWiFS Rrs employing TSM empirical local algorithm proposed by Siswanto et al. (2011).

2.1.3. Satellite Data Analysis

Sub-setting ocean color and SST satellite data to the marginal seas (Figure 1) was accomplished by using Unix-based SeaDAS version 6.4, whereas sub-setting satellite WS, RR, and reanalyzed SSS data was carried out by using Matrix Laboratory (MATLAB) software. Because clouds interfere with SeaWiFS optical and thermal sensors, satellite-retrieved Chl-a, AOT, and SST datasets include pixels with no data. Before conducting analyses of spatial and temporal variations, we reconstructed data missing due to cloud cover by using empirical orthogonal function-based data interpolation (DINEOF) to produce cloud-free satellite Chl-a, AOT, and SST datasets. DINEOF is a non-parametric EOF-based method for reconstruction of missing data or blank pixels (Alvera-Azcarate, et al., 2007). DINEOF was applied by first reconstructing time series satellite data into a three-dimensional matrix. The first two dimensions were spatial dimensions (latitude and longitude), and the third dimension was time (number of months). The missing values in each satellite image were set to not-a-number (NaN). A Singular Value Decomposition technique was then applied to reconstruct the NaN pixels while computing the EOFs of the matrix.

To make AVHRR and MODIS SSTs comparable, MODIS SSTs were linearly regressed against AVHRR SSTs at each pixel. Linear regression was conducted separately on a monthly basis within the period when both AVHRR and MODIS SSTs were available (May 2002 to December 2009). For each month, the regression coefficients (slope and intercept) at each pixel were then used to convert MODIS SSTs to values compatible with AVHRR SSTs. Finally, we used AVHRR SSTs from September 1997 to December 2009 and MODIS SSTs from January 2010 to December 2010 to construct 13-year, satellite-derived SST datasets.

Pixel-based non-parametric correlations of SeaWiFS Chl-a on the other satellite-retrieved variables were used to derive correlation coefficients (with statistical significance) and to identify relationships. To identify possible impacts of large-scale climatic anomalies associated with IOD and ENSO on interannual variations of SeaWiFS Chl-a, Chl-a anomalies were compared to the Dipole Mode Index (DMI, http://www.jamstec.go.jp/frcgc/research/d1/iod/e/index.html) and Nino3.4 SST anomalies (Nino3.4, http://www.cpc.ncep.noaa.gov/data/indices/ sstoi.indices). The DMI is an anomalous SST gradient between the western (50–70°E and 10°S to 10°N) and southeastern (90–

110°E and 10°S–0°N) equatorial Indian Ocean and is used to identify the phase of an IOD event. The Nino3.4 is an ENSO phase indicator derived by averaging SST anomalies in the region bounded by 5°N to 5°S and 170–120°W.

To assess trends in Chl-a concentrations, we used the Chl-a anomaly, which was derived by removing the seasonal cycle of Chl-a from the Chl-a time series. However, when assessing interannual variations of Chl-a, we derived the Chl-a anomaly differently. We first removed the seasonal cycle of Chl-a from the Chl-a time series and then removed the trend. This metric of Chl-a interannual variation was therefore not confounded by seasonal cycles and long-term trends. There remained only the signature of interannual variability associated with large-scale climatic anomalies. Relationships between the Chl-a anomaly and anomalies of other variables were investigated to discern the variables that probably accounted for the Chl-a interannual variations. Anomalies of other satellite-retrieved environmental variables were also derived using the same procedure.

2.2. Numerical Modeling for Researches in the Gulf of Thailand and the South China Sea

2.2.1. Circulation Model

Princeton Ocean Model (POM) is used to simulate three-dimensional circulation. The governing equations of the model include conservation of mass and momentum, salinity, temperature and turbulence equations under the hydrostatic and Boussinesq approximations. The equations are written in a bottom-following, sigma coordinate system where vertical layers are scaled according to bottom topography. More details of the POM, including a mathematical description, are contained in Mellor (1998).

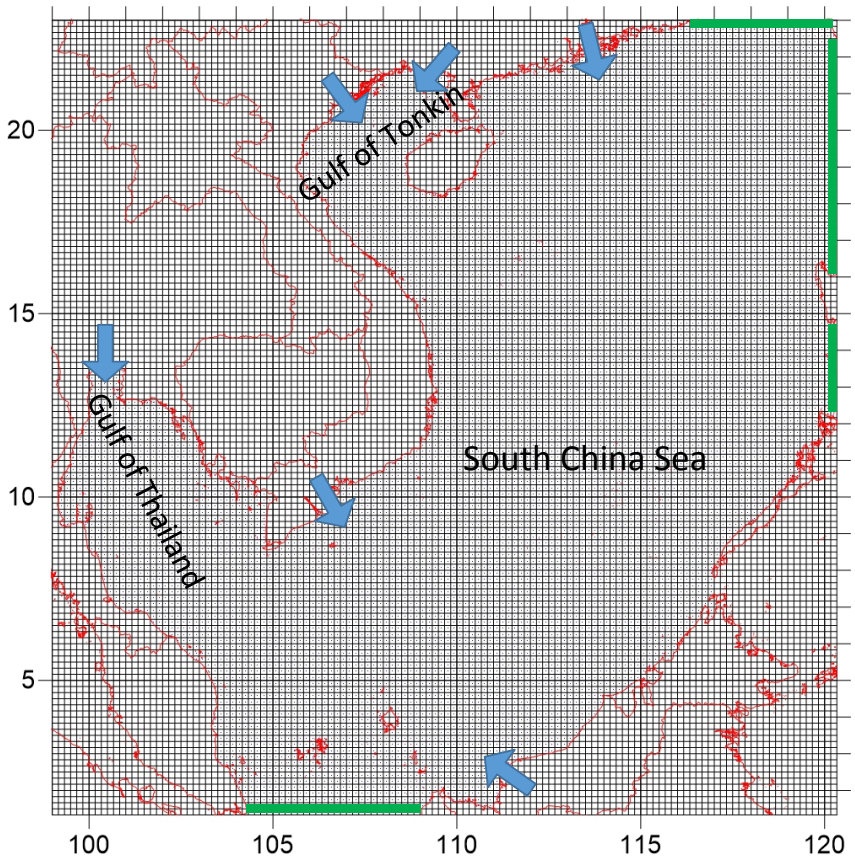

Figure 2 Computational domain for numerical experiments. Light blue arrows and green lines represent major rivers and open boundaries, respectively.

To apply the circulation model to the SCS, it was divided horizontally into 128 × 130 grids in spherical coordinates with grid spacing 10 × 10 minutes in latitude and longitude, respectively (Figure

2). The vertical domain was set to 25 σ-levels with logarithmic portions. The model uses bathymetry data from NOAA National Geophysical Data Center (NGDC), GEBCO30 (http://www.gebco.net). Salinity and temperature profiled data were obtained from NODC World Ocean Atlas 2001 (WOA 2001). Monthly means of discharges of major rivers around the SCS, previously reported in several publications (Mekong River Commission, 2009; Gao et al., 2013; Staub et al., 2000), used to derive boundary conditions at the river mouths. Monthly averaged winds of QuikScat (http://www.ssmi.com) were used as an important surface driving force. Tidal currents, as water elevations calculated using harmonic analysis, were set to drive the water system through the sea boundary. Four tidal constituents, namely K1, O1, M2 and S2, were considered in harmonic analysis where their amplitudes and phases were extracted from Fang et al. (1999) (Table 1). The open boundaries for salinity, temperature, and turbulence parameters were set by a condition called "upstream advection" as defined in Equation 1 (Mellor, 1998):

$$\frac{\partial T}{\partial t} + U\,\frac{\partial T}{\partial x} = 0\,, \qquad (1)$$

where T is referred to those parameters; U and x are velocity and length perpendicular to the boundary, respectively; and t is time. Salinity and temperature are observed values which were fixed throughout model operation.

Table 1. Tidal constituents used to calculate tidal elevation at the open boundaries.

Station	Latitude (°N)	Longitude (°E)	M2		S2		K1		O1	
			Amp (cm)	Phase (deg)	Amp (cm)	Phase (deg)	Amp (cm)	Phase (deg)	Amp (cm)	Phase (deg)
Pulau Tioman	2°48′	104°08′	58	274	18	327	49	25	34	343
Tanjong Datu	2°05′	109°39′	91	117	18	141	37	335	15	256
Kulion I.	11°48′	119°57′	24	303	9	4	30	318	30	268
Olongapo	14°49′	120°17′	17	287	6	324	27	316	25	267
San Fernando	16°37′	120°18′	8	264	2	283	24	312	20	267
Kaohsiung	22°37′	120°16′	15	236	6	248	16	295	15	249
Shanwei	22°45′	115°21′	28	255	11	278	33	298	26	250
Kaohsiung	22°37′	120°16′	15	236	6	248	16	295	15	249

The model is operated using a technique called the robust diagnostic (Yanagi, 1999), where damping terms are introduced to the temperature and the salinity equations. These additional terms are γ (T^* − T) and γ (S^* − S), respectively. Here, γ is called the nudging constant (= ΔT_i /(86,400 s × 5)); ΔT_i is internal time step (50 s); and T^* and S^* are the observed water temperature and salinity, respectively. In POM operation, the damping terms are added in the process of data updates before going to the next round of calculation.

The model was set to have no momentum fluxes generated by exchanges of heat and salt from the atmosphere or sea bottom because they are considered to be insignificant when compared to wind, discharges and tide. Seawater state was set at rest at the initial time of model operation (t = 0). Time steps were 5 s and 50 s for the external and the internal modes, respectively. The model was driven by all driving forces from the start until a quasi-steady state was reached at day 20, which is determined by checking the series of averaged kinetic energy.

2.2.2. Ecosystem Model

The ecosystem model of five compartments, including phytoplankton (P), zooplankton (Z), detritus (D), DIN (N_N) and DIP (N_P), is incorporated into five governing equations (Guo and Yanagi, 1998), expressed in a Cartesian coordinate system, shown as follows:

$$\frac{\partial P}{\partial t} + \vec{V}\cdot\nabla P + S_P\frac{\partial P}{\partial z} = DIF\ (P) + A_1 P - R_1 P - A_2 P^2 - A_3 Z\,, \qquad (2)$$

$$\frac{\partial Z}{\partial t} + \vec{V}\cdot\nabla Z = DIF\ (Z) + A_3 Z - A_4 Z^2 - A_5 Z - A_6 Z\,, \qquad (3)$$

$$\frac{\partial D}{\partial t} + \vec{V} \cdot \nabla D + S_d \frac{\partial D}{\partial z} = DIF(D) + A_2 P^2 + A_4 Z^2 + A_6 Z - A_7 D\,, \tag{4}$$

$$\frac{\partial N_N}{\partial t} + \vec{V} \cdot \nabla N_N = DIF(N_N) - A_1 P + A_6 Z + A_7 D\,, \tag{5}$$

$$\frac{\partial N_P}{\partial t} + \vec{V} \cdot \nabla N_P = DIF(N_P) - A_1 P + A_6 Z + A_7 D\,, \tag{6}$$

where

$$\vec{V} \cdot \nabla() = u \frac{\partial}{\partial x} + v \frac{\partial}{\partial y} + w \frac{\partial}{\partial z}\,, \tag{7}$$

$$DIF() = \frac{\partial}{\partial x}\left(K_h \frac{\partial}{\partial x}\right) + \frac{\partial}{\partial y}\left(K_h \frac{\partial}{\partial y}\right) + \frac{\partial}{\partial z}\left(K_v \frac{\partial}{\partial z}\right). \tag{8}$$

Here $\vec{V}$ is three-dimensional velocity composed of u, v, and w, which are velocity components in x, y and z directions, respectively; x and y are axes in the horizontal plane, and z is that in the vertical direction; t is time; and K_h and K_v are horizontal and vertical diffusivities, respectively. Velocity and diffusivity data used in the ecosystem model are the results of POM computed in the same time step. S_p and S_d, sinking speeds of phytoplankton and detritus, respectively, are set as constants. The biochemical terms are described below, and all relevant parameters are summarized in Table 2.

Table 2. Parameters used in the ecosystem model and their references.

Definitions	Symbols	Values	Units	Reported values	References
Maximum photosynthetic rate at 0℃	V_m	1.5	day^{-1}	0.05 – 8.10	Parson et al. (1984)
Half saturation constant for DIN	K_{SN}	1.0	μmol-N l^{-1}	0.04 – 4.21	Parson et al. (1984)
Half saturation constant for DIP	K_{SP}	0.05	μmol-P l^{-1}	0.008 – 0.530	O'Conner et al. (1975)
Optimum light intensity for phytoplankton	I_{opt}	16.0	$MJ/m^2/day$	1.8 – 12.0	Parson et al. (1984)
Coefficient	k_T	7.9964			
Respiration rate of phytoplankton at 0℃	R_0	0.02	day^{-1}	0.030 – 0.051	Di Toro et al. (1971)
Natural mortality rate of phytoplankton at 0℃	M_p	0.03	(μmol-N l^{-1}.day)$^{-1}$	0.04	Onisuka and Yanagi (2005)
Maximum grazing rate of zooplankton at 0℃	R_{max}	0.3	day^{-1}	0.3	Kawamiya et al. (1995)
Ivlev constant	λ	0.47	$(mgChl\text{-}a/m^3)^{-1}$	0.47	Smayda (1973)
Threshold of phytoplankton in grazing	P^*	0.05	$mgChl\text{-}a/m^3$	0.08 – 0.09	Kawamiya et al. (1995)
Natural mortality rate of zooplankton at 0℃	M_z	0.06	(μmol-N $l^{-1}day)^{-1}$	0.06	Kawamiya et al. (1995)
Assimilation efficiency of zooplankton	α_z	0.7		0.7	Onisuka and Yanagi (2005)
Growth efficiency of zooplankton	β_z	0.3		0.3	Onisuka and Yanagi (2005)
Bacterial decomposition rate pf detritus at 0℃	V_{PN}	0.05	day^{-1}	0.05	Fasham et al. (1990)
Sinking velocity of phytoplankton	S_p	10	cm day^{-1}	33	Smayda (1970)
Sinking velocity of detritus	S_d	100	cm day^{-1}	100	Yanagi et al. (1993)

Phytoplankton growth rate A_1 is decided by:

$$A_1 = V_m k_T \min\{V_1(N_N), V_1(N_P)\} \cdot V_2(I)\,, \tag{9}$$

$$V_1(N_N) = \frac{N_N}{K_{SN} + N_N}\,, \tag{10}$$

$$V_1(N_P) = \frac{N_P}{K_{SP} + N_P}\,, \tag{11}$$

$$V_2(I) = \frac{I}{I_{opt}} \exp\left(1 - \frac{I}{I_{opt}}\right), \tag{12}$$

Considered in terms of the Redfied ratio, most observed N/P mole ratios of over 16 indicate that DIP might be the limiting nutrient. The model, however, allows both nutrients to control phytoplankton growth, depending on their simulated concentrations in the computational domain. I is the light intensity at a given depth which is expressed as:

$$I(z) = I_s \exp\left[-\int_0^z k(z)\,dz\right], \quad (13)$$

$$k(z) = 0.04 + 0.054\,C(z)^{\frac{2}{3}} + 0.0088\,C(z), \quad (14)$$

$$C(z) = P(z) + \delta(Z(z) + D(z)), \quad (15)$$

where I_s denotes the light intensity at the sea surface; k is the extinction coefficient; and C is the concentration of chlorophyll-a. Self-shading, a phenomenon contributing to decreased underwater light resulting from suspended plankton cells and other organic particles, is represented by Equation 14 (Riley, 1956). Not only phytoplankton, but also zooplankton and detritus are considered in the self-shading effect (Equation 15), where δ is a constant representing the contribution of those non-algal particles. It should be added that the water column near the river mouths is quite turbid, with strong seasonal variations following river discharge, monsoonal wind and current. The influence of water turbidity, together with phytoplankton, zooplankton and detritus, on the extinction coefficient, however, has not yet been reported for the SCS area. Lacking such information, the functions reported in another study were employed.

The coefficient k_T is derived from a function $\exp(k_0 \cdot T)$, where k_0 is a constant 0.0693 (Kawamiya et al., 1995) and T is water temperature in °C. Here T was set to 30 °C, which is consistent with observed data; therefore, k_T = 7.9964. k_T is based on the rate of change of photosynthesis to temperature (Eppley, 1972). It was also adopted for other physiological processes that depend on temperature, as shown below. This application has successfully been applied in several studies, such as those of Kawamiya et al. (1995); Onitsuka et al. (2007).

The respiration rate of phytoplankton R_1:

$$R_1 = k_T R_0. \quad (16)$$

The natural mortality rate of phytoplankton A_2:

$$A_2 = k_T M_p. \quad (17)$$

The grazing rate of zooplankton A_3:

$$A_3 = k_T R_{\max}\left[1 - \exp\lambda(-P + P^*)\right]. \quad (18)$$

When phytoplankton concentration (P) is smaller than the threshold of phytoplankton in grazing (P*), A_3 is set to zero, which means phytoplankton will not be eaten if its concentration is below the grazing threshold.

The natural mortality rate of zooplankton A_4:

$$A_4 = k_T M_z. \quad (19)$$

The production rate of fecal pellets of zooplankton A_5:

$$A_5 = (1 - \alpha_z) \cdot A_3. \quad (20)$$

The generation rate of urine of zooplankton A_6:

$$A_6 = (\alpha_z - \beta_z) \cdot A_3. \quad (21)$$

The decomposition rate of detritus A_7:

$$A_7 = k_T V_{PN}. \quad (22)$$

Because relevant parameters, especially the physiological properties of plankton in the study area, have rarely been reported, it was necessary to use data measured in other regions, or as applied to other ecosystem model experiments. Table 2 summarizes parameters used in the ecosystem model, with their previously reported values and references. Most are in ranges of the reported values but some are not, due to the need to keep the results of the chlorophyll-a concentration within observed ranges.

The loads of DIN and DIP of major rivers were taken from many references including Liu et al. (2009); Wosten et al. (2003); NOAA National Oceanographic Data Center (NODC); World Ocean Atlas 2009 (WOA2009) (http://www.nodc.noaa.gov) and Buranapratheprat et al. (2008b). Non-point source nutrients along coastlines were ignored due to a lack of reliable data. For the sea boundary,

chlorophyll-a, DIN and DIP at all cross-sectional grids were derived from extrapolation and interpolation of data of the stations close to the boundary line. Data from NODC and WOA2009 were used in this case. Chlorophyll-a at the river mouths and the open boundaries are estimated from Li et al. (2013); Naik and Chen (2008); Shang et al. (2012); MODIS satellite data (http://oceancolor.gsfc.nasa.gov); Buranapratheprat et al. (2008b). Averaged solar radiation measured at Bangkok meteorological station was used as the radiation over SCS to calculate underwater light intensity (Equation 13). The model also needed phytoplankton and detritus data at the open boundary, but neither data were available. Based on energy transfer in the trophic level system (Nybakken and Bertness, 2004), which is also applied to the biomass, zooplankton was assumed to be 10 % of phytoplankton biomass while organic detritus was assumed to be equal to phytoplankton biomass. These assumptions were also applied at the river boundaries and initial conditions of model simulation.

The computational domain, grid spacing and time steps were the same as those of POM. Lateral sea boundary conditions of ecosystem parameters were the same as those of temperature and salinity with fixed values at all grid locations along the boundary plane throughout model operation. Exchange fluxes of those parameters at the sea surface and bottom boundaries were not permitted because they were unknown, but were assumed to be small compared to the river loads. However, they were set to be recycled in the system until transported out through the sea boundary. Initial values of ecosystem parameters, derived from the overall average of measured data, were set to be identical in all experiments. Zooplankton and detritus were assigned as 10 % of chlorophyll-a and equal to chlorophyll-a concentrations, respectively, similar to the lateral boundary setting. The model operation was tested and a steady state of all simulated parameters was attained after days 10 of computation. Calculated results were collected and averaged from days 20 to 50 in the same way as those of circulation model. Simulated chlorophyll-a distributions in the same months of observational cruises are presented and discussed.

2.2.3. Water Column Analysis

Water column conditions, if stratified or well mixed, are investigated by considering the mean rate of change of potential energy of water column (dV/dt) (Equation 23). Simpson and Bowers (1981) introduced four significant environmental factors including surface heating, freshwater inputs, tidal and wind stirrings. In this study, however, the buoyancy from atmospheric exchanges (Precipitation (P) and Evaporation (E)) is treated as a significant freshwater source in the analysis. The governing equation is shown as the follow.

$$\frac{dV}{dt} = -\frac{\alpha g Q H}{2C_p} - \frac{\beta g S H (R + P - E)}{2A} + \frac{4\varepsilon k_b \rho_w U_t^3}{3\pi} + \delta k_s \rho_a W^3 \qquad (23)$$

The first two terms on the right hand side represent the influences of buoyancy forces including surface heating, freshwater inputs from river discharge and atmospheric water exchanges, respectively. The third and the forth terms denote the effects of tidal and wind stirrings, respectively. Positive and negative signs are correspondingly assigned to the terms that increase and decrease vertical water column mixing. All constants together with their definitions, values and units are summarized in Table 3.

Table 3. Parameters used for the calculation of the rate of change of potential energy in water column.

Symbols	Definitions	Values	Units
α	Thermal expansion coefficient	2.3×10^{-4}	$^{o}C^{-1}$
g	Gravitational acceleration	9.8	m s^{-2}
H	Water depth		m
Q	Heat flux		W m^{-2}
C_p	Specific heat of water	0.95	Cal g^{-1} $^{o}C^{-1}$
β	Salinity contraction to density	0.001	g cm^{-3} psu^{-1}
S	Salinity		psu
R	River discharge		m^3 s^{-1}
P	Precipitation		m^3 s^{-1}
E	Evaporation		m^3 s^{-1}
A	Surface area under river discharge influence		m^2
ε	The efficiency of conversion from turbulence to potential energy for tidal stirring	0.015	
k_b	Bottom drag coefficient	2.5×10^{-3}	
ρ_w	The density of seawater	1.02	g cm^{-3}
U_t	Tidal magnitude		m s^{-1}
δ	The efficiency of conversion from turbulence to potential energy for wind stirring	0.039	
C_D	Surface drag coefficient (Eq. 3)		
k_s	$C_D \times \gamma$		
γ	The ratio of wind-induced current to wind speed	0.0127	
ρ_a	The density of air	1.25×10^{-3}	g cm^{-3}

It should be addressed here that surface drag coefficient is treated as a variable due to its sensitivity to wind magnitude (Stewart, 2006). The coefficient equations, developed by Yelland and Taylor (1996) based on the relationship between wind magnitude at 10 m above sea surface (W_{10}) and surface drag coefficient (C_D) are used as the follows.

$$1000\,C_D = 0.29 + \frac{3.1}{W_{10}} + \frac{7.7}{W_{10}^2}, \qquad (3 \le W_{10} \le 6 \text{ m s}^{-1}) \qquad (24a)$$

$$1000\,C_D = 0.60 + 0.071 W_{10}, \qquad (6 \le W_{10} \le 26 \text{ m s}^{-1}) \qquad (24b)$$

Temperature and salinity data are from NODC World Ocean Atlas 2001 (WOA 2001). They are used to calculate water density in terms of Sigma-t. Air-sea heat exchanges consider 4 terms including short wave radiation (SWR), long wave radiation (LWR), sensible heat flux (SHF) and latent heat flux (LHF). The data are provided by the School of Marine Science and Technology, Tokai University, available through http://dtsv.scc.u-tokai.ac.jp/j-ofuro/. They have previously been used to analyze annual surface heat fluxes in the GoT by Luadnakrob and Buranapratheprat (2012). Monthly wind data from QuickScat (http://www.remss.com/) are used to calculate wind stirring. Monthly river discharge data (Figure 3) are from Royal Irrigation Department, Thailand. Annual discharge of available data for all major rivers surrounding GoT is about 57 km^3. This value, however, is a half smaller than total discharge and runoff estimated based on all related discharge basin by Stransfield and Garrett (1997) (129.5 km^3). The discharge data of our study are therefore doubled in the analysis (114 km^3). Since the nature of discharge data are lateral characteristic, they are weightily distributed over the surface area based on a criteria that low surface salinity area should receive larger discharge than high surface salinity area. Precipitation and evaporation gridded data over the GoT, provided by Woods Hole

Oceanographic Institution available at http://oaflux.whoi.edu, are used to calculate net atmospheric freshwater flux (P – E). Average net atmospheric water exchanges for each month are shown in Figure 4. Tidal data as the amplitude of $M_2 + K_1$ are from the results of a numerical simulation by Yanagi and Takao (1998).

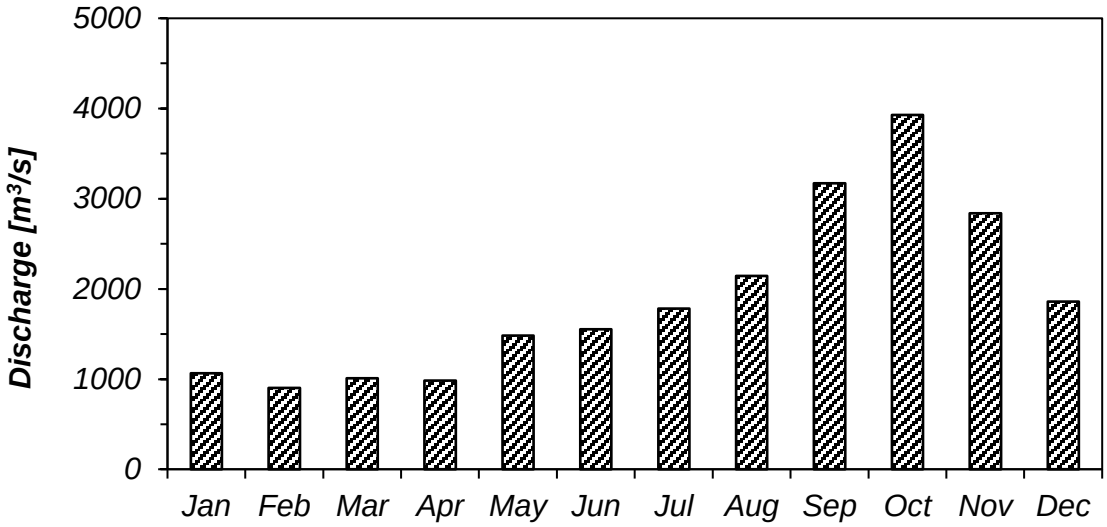

Figure 3. Average monthly river discharges into the Gulf of Thailand (source: the Royal Irrigation Department of Thailand).

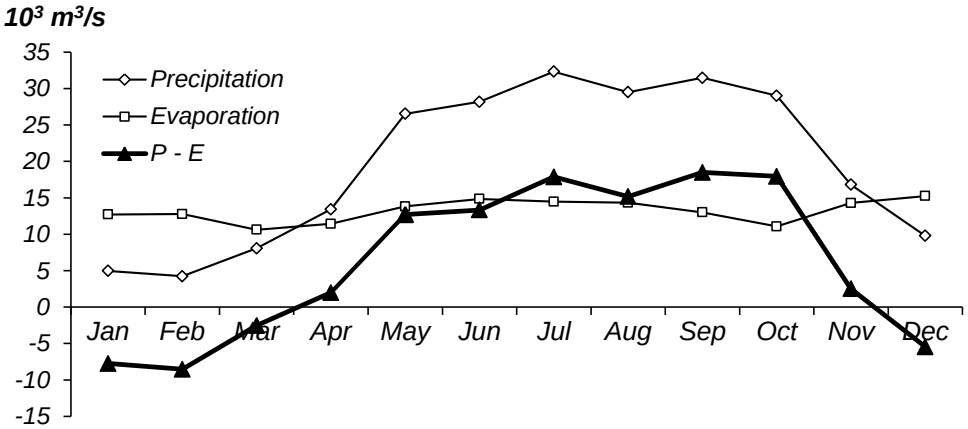

Figure 4. Average monthly atmospheric freshwater fluxes over the Gulf of Thailand (source: http://oaflux.whoi.edu/).

3. Results & Discussion

3.1. Application of Satellite Observations to Study Spatial and Temporal Chl-a Variations

3.1.1. Chl-a Seasonal Cycle, Interannual Variation, and Decadal Trend in the Strait of Malacca

The SM was divided into three regions (north, middle and south) due to physical oceanographic and water optical properties as detailed in Siswanto and Tanaka (2014) (Figure 5). Over the entire region of the SM, a remarkable seasonal cycle of Chl-a concentrations was apparent; concentrations were high during the NEM (Figure 6a) and low during the SWM (Figure 6c). A distinct seasonal variation of monthly climatological means of Chl-a was apparent in all three regions of the SM. The time series

of SeaWiFS data from 1997 to 2010 revealed a seasonal peak of Chl-a in the southern region during October (Figure 6m), consistent with the results of Tan et al. (2006), which were based on a shorter time series of SeaWiFS Chl-a data (1997–2003).

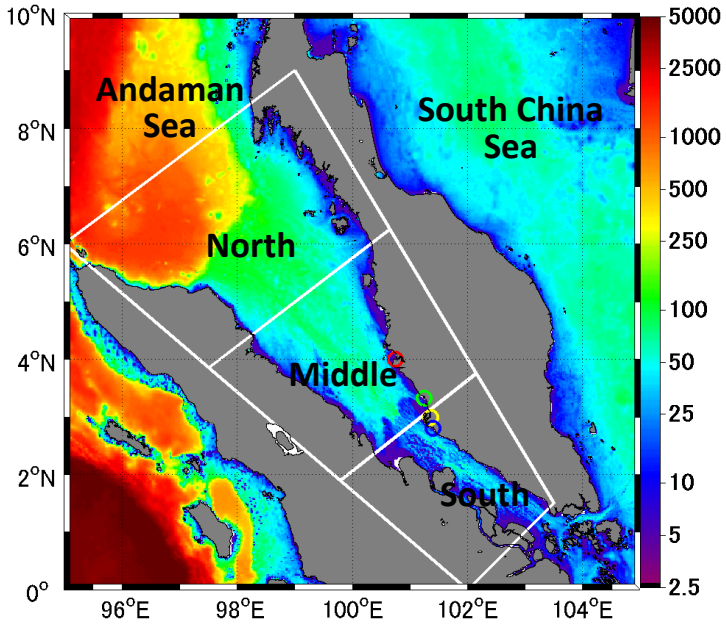

Figure 5. Map of the SM divided into northern, middle, and southern regions. Color scale indicates depth (m) of the water column. Red, green, yellow, and blue circles along the western coast of Peninsular Malaysia indicate the estuaries of the Perak, Selangor, Klang, and Langat rivers, respectively.

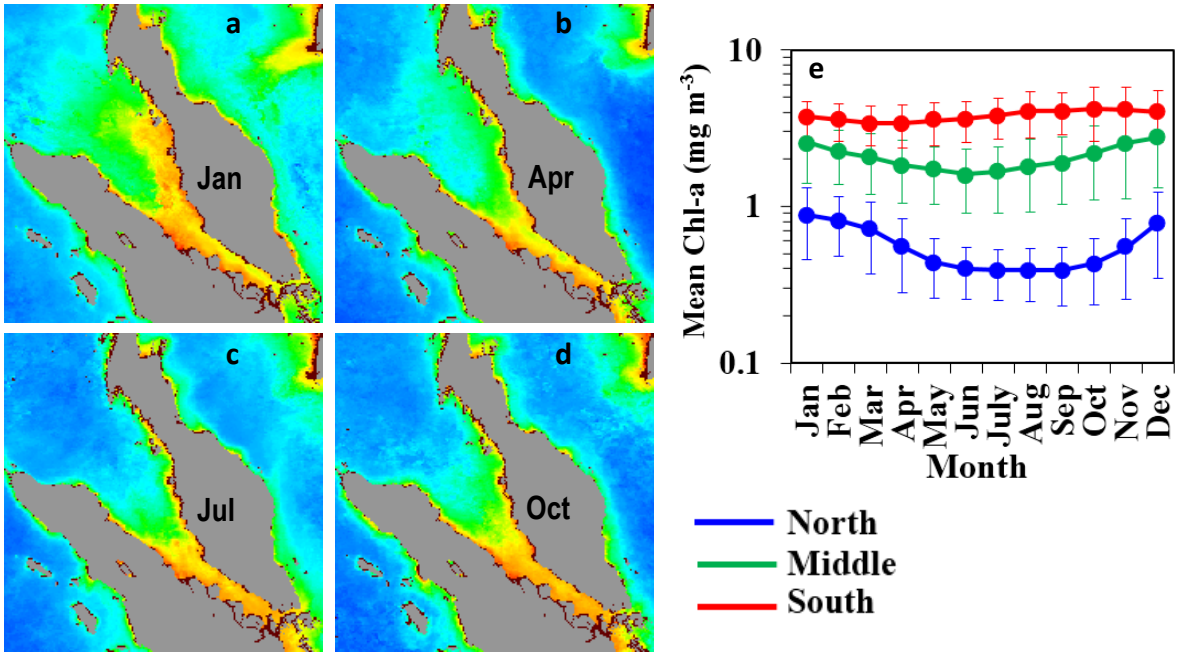

Figure 6. Monthly climatological means of SeaWiFS Chl-a (mg m^{-3}) averaged from monthly SeaWiFS Chl-a data (September 1997 to December 2010) for January, April, July, and October. (m) Spatial means of monthly climatological SeaWiFS Chl-a in the northern, middle, and southern regions of the SM. Vertical bars in (m) indicate standard deviations around the SeaWiFS Chl-a means.

Although the Chl-a seasonal cycles were similar in the northern and middle regions, those two regions were remarkably different in terms of monthly climatological means and ranges of variation (quantified in terms of standard deviations) of Chl-a concentrations. The peak of the Chl-a bloom during the NEM also occurred earlier in the middle region (in December) than in the northern region (in January). Tan et al. (2006) missed this meridional difference in the timing of the peak of the Chl-a bloom during the NEM, because they combined both the northern and middle regions of our study into their single northern region. It is obvious from our study that the highest concentrations of Chl-a during the NEM tend to occur progressively earlier from the northern to the southern regions.

A statistically significant negative correlation (< -0.4, $p < 0.05$) between Chl-a and SST was apparent over a wide area within the northern and middle regions of the SM (area A in Figure 7a). There was almost no significant relationship between Chl-a and AOT (Figure 7b). There was a very significant negative correlation (< -0.4, $p < 0.05$) between RR and Chl-a in the northern region of the SM (Figure 7c). This significant negative correlation extended to the Andaman Sea, whereas in the SM middle and southern regions, there was almost no association between Chl-a and RR.

An east-west, belt-like pattern of significant positive correlation (> 0.5, $p < 0.05$) between Chl-a and WS was apparent approximately in area A (Figure 8a). There was no significant correlation between Chl-a and WS within a large portion of the middle region of the SM and northern part of the northern region of the SM. There was a significant negative correlation (< -0.5, $p < 0.05$) between U and Chl-a in the northern region of the SM (Figure 8b). However, a significant positive correlation coefficient (> 0.3, $p < 0.05$) was apparent in some pixels near the coastal regions (area Z). Like U, V also showed a significant negative correlation with Chl-a (< -0.3, $p < 0.05$) in the northern region of the SM (Figure 8c). In the Peninsular Malaysian coastal area of the middle region of the SM (area Z), a significant negative correlation was also observed. The negative correlation between SST and Chl-a implies that SST was not a factor that drove the Chl-a seasonal cycle. The negative correlation between Chl-a and SST contradicts the basic tenet of temperature-dependent phytoplankton growth (e.g., Eppley, 1972). The negative correlation between Chl-a and SST, however, may be indicative of nutrient-limited phytoplankton growth (Behrenfeld and Falkowski, 1997).

The seasonal cycles of Chl-a in the northern and middle regions of the SM must therefore be associated with seasonal cycles of nutrient fluxes. Nutrients can be supplied by vertical fluxes (by dry or wet atmospheric deposition and by deep water upwelling/mixing) and from horizontal nutrient fluxes (loading by RD). Considering the weak correlation between Chl-a and AOT (Figure 7b) and the negative correlation between Chl-a and RR (Figure 7c), a role of atmospheric dry and wet deposition as nutrient sources in controlling the seasonal Chl-a cycle can be ruled out. Hence, there are two possible sources of nutrients that may drive the seasonal cycle of Chl-a, namely, vertical fluxes from deep layers and/or horizontal fluxes from RD.

The significant negative correlations between U and Chl-a and between V and Chl-a in the northern region of the SM (Figure 8b,c) reflect the seasonal coupling between high Chl-a and the strong northeasterly winds that occur during the NEM, and between low Chl-a and the weak southwesterly winds that occur during the SWM. Strong northeasterly winds during the NEM may increase the Chl-a in the northern region of the SM in two ways: (1) by increasing the flux of nutrients to surface waters through water column vertical entrainment, and (2) by northwestward horizontal advection of high-Chl-a water from the middle region of the SM via wind-driven Ekman transport Tan et al. (2006). This northwestward Ekman transport probably accounts for fact that the Chl-a bloom occurs earlier in the middle region (December) than in the northern region (January) (Figure 6e). The low Chl-a in the northern region of the SM during the period of weak southwesterly winds may reflect the small amount of water column upward entrainment of nutrients as well as southeastward advection of low-Chl-a water from the Andaman Sea via Ekman transport (Ibrahim and Yanagi, 2006). The high Chl-a during the NEM in the middle region of the SM was caused mainly by the increase of Chl-a along the coast of Peninsular Malaysia. One of the possible mechanisms underlying this coastal Chl-a increase is wind-driven coastal upwelling, the evidence for which is the significant negative correlation between V and Chl-a in the coastal area of Peninsular Malaysia (area Z, Figure 8b,c).

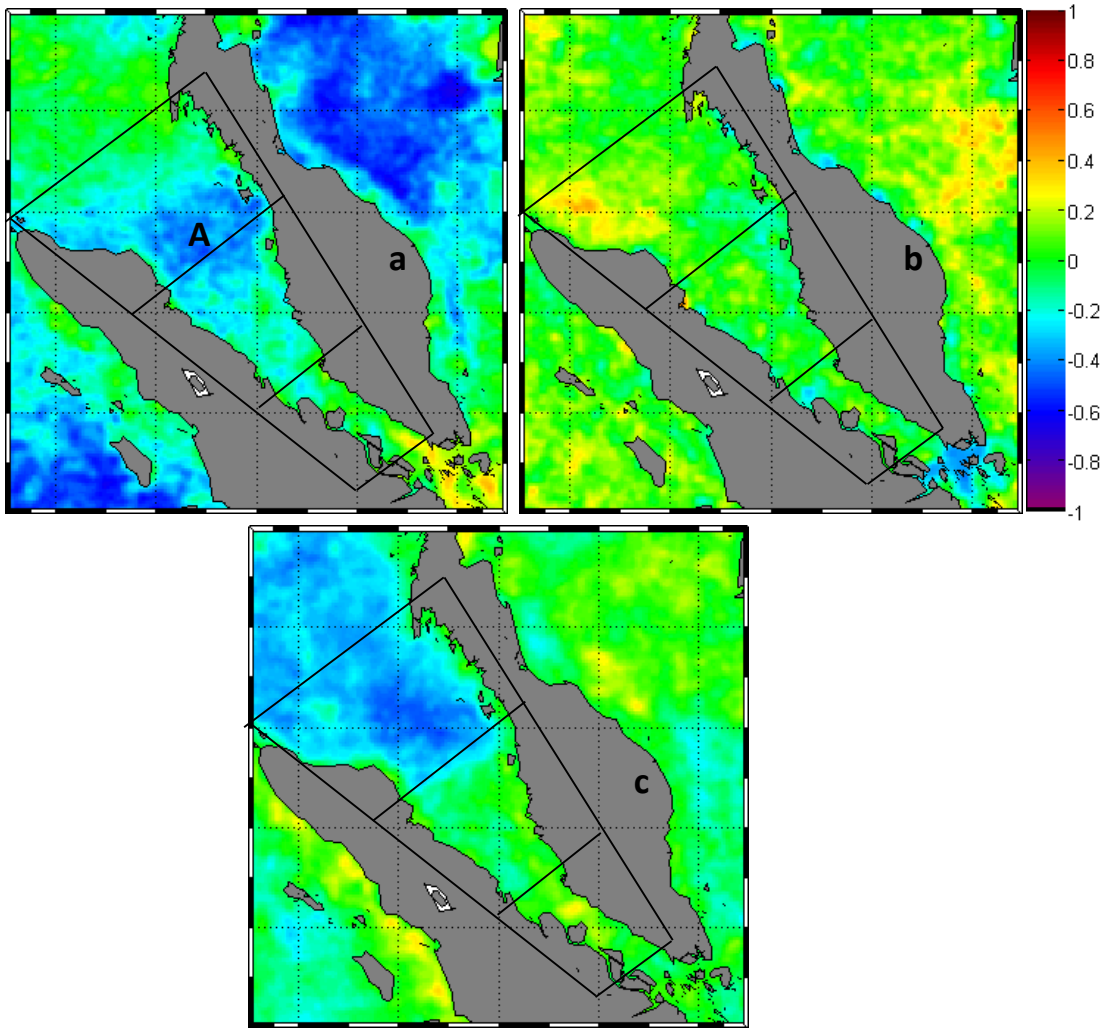

Figure 7. Spatial variations of the correlation coefficient derived from linear regressions of SeaWiFS Chl-a on AVHRR/MODIS SST (a), SeaWiFS AOT (b), and TRMM RR (c). The letter A in (a) indicates the area with significant negative correlation between Chl-a and SST.

The monthly climatological mean of RD was highest in November, especially in the cases of the Perak, Selangor, and Langat rivers (Figure 9a). The average RR over Peninsular Malaysia was also highest during November (see Siswanto and Tanaka, 2014). High RR during the NEM inevitably increases freshwater discharge into the SM, as evidenced by the minimum of surface salinity during the NEM (see Amiruddin et al., 2011). Besides transporting freshwater, RD also transports nutrients from the land into the SM. A significant positive correlation (> 0.5, $p < 0.05$) between monthly climatological Chl-a and monthly climatological RD (average for the four main rivers, Figure 9b,c) in approximately the same area of RD-diluted, low-salinity water (see Amiruddin et al., 2011), may reflect the role of the seasonality of RR in determining seasonal Chl-a variations in the SM through the influx of nutrients from the land. Besides coastal upwelling, high RD in November from Peninsular Malaysia may also have been an important source of allochthonous nutrients from the land. The significant positive correlation between monthly climatological means of RD and Chl-a in the coastal area adjacent to the river estuaries is consistent with this hypothesis (Figure 9b,c).

During the SeaWiFS full mission, the Chl-a anomaly (seasonality-removed Chl-a anomaly) tended to increase, both in the middle and southern regions. The rates of increase or slopes were about 0.004 mg m^{-3} mo^{-1} and 0.007 mg m^{-3} mo^{-1}, respectively, or about 0.05 mg m^{-3} yr^{-1} and 0.08 mg m^{-3} yr^{-1}, respectively (Figure 10a,b). The trend of increasing Chl-a in the middle region was likely due

more to the increasing trend of Chl-a in the southeastern part of the middle region (Figure 10a), where the rate of change was greater than 0.005 mg m^{-3} mo^{-1} or 0.06 mg m^{-3} yr^{-1}. In the northern region of the SM, however, despite a conspicuous Chl-a seasonal cycle, almost no trend of Chl-a was apparent in the last decade of SeaWiFS.

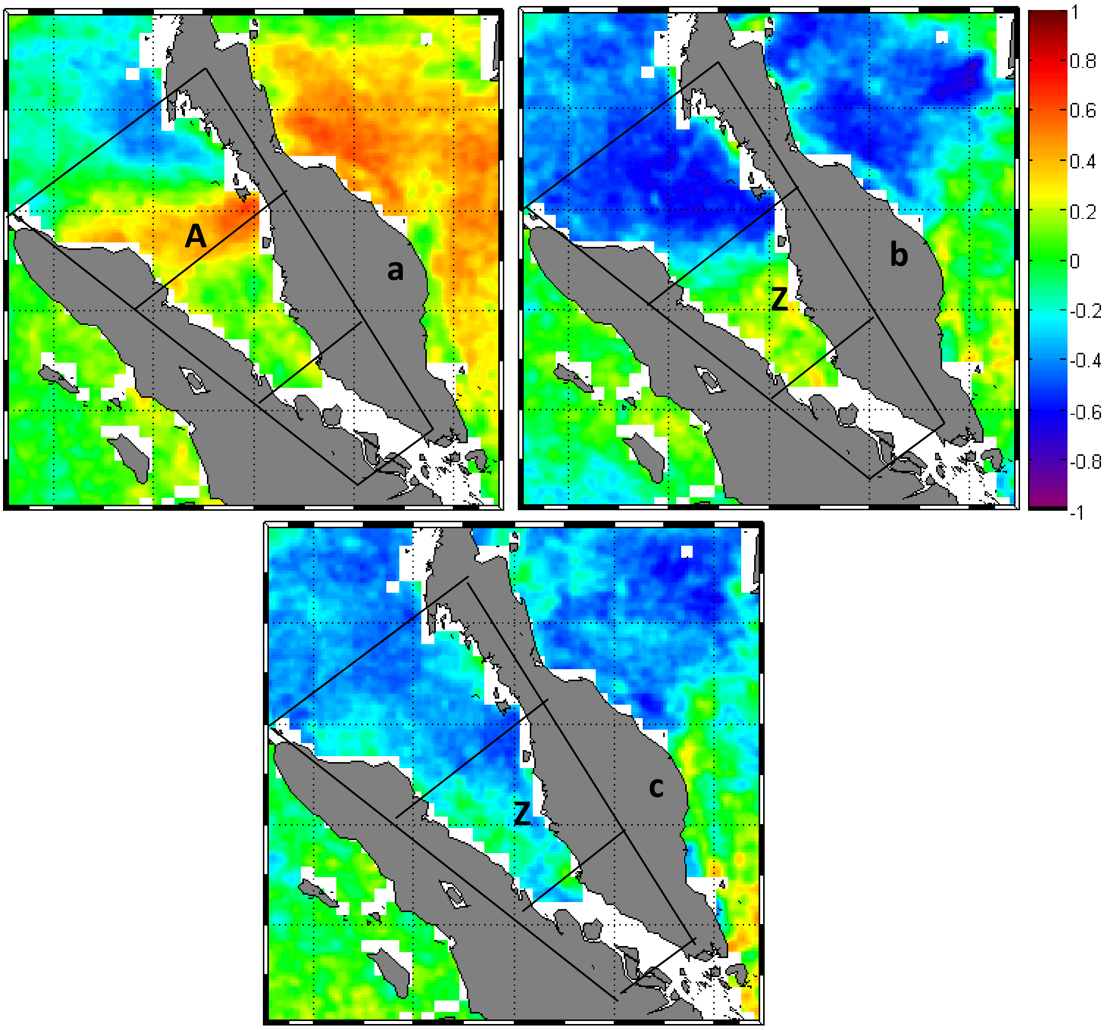

Figure 8. Spatial variations of the correlation coefficient derived from linear regressions of SeaWiFS Chl-a on QuikScat WS (a), U (b), and V (c). The southern region is masked out, because there was no wind field retrieval. The letter A in panels (a) indicates the areas where there was a significant positive correlation between Chl-a and WS. The letter Z in panels (b,c) indicates the coastal region where there was a significant correlation between Chl-a and wind components.

The trend during the last decade of SeaWiFS Chl-a in the southern region of the SM may reflect trends of other variables (e.g., inorganic suspended sediment, gelbstoff), which are likely to cause incorrect Chl-a retrieval by the NASA standard ocean color algorithm. However, environmental variable anomalies of SST, AOT, RR, and WS showed no significant trends (all correlation coefficientare ≤0.1, $p > 0.1$, Figure 11). Therefore, other uninvestigated variables, the trends of which were independent of the trends of the investigated environmental variables, may have been responsible for the trend of increasing SeaWiFS Chl-a in the southern region of the SM.

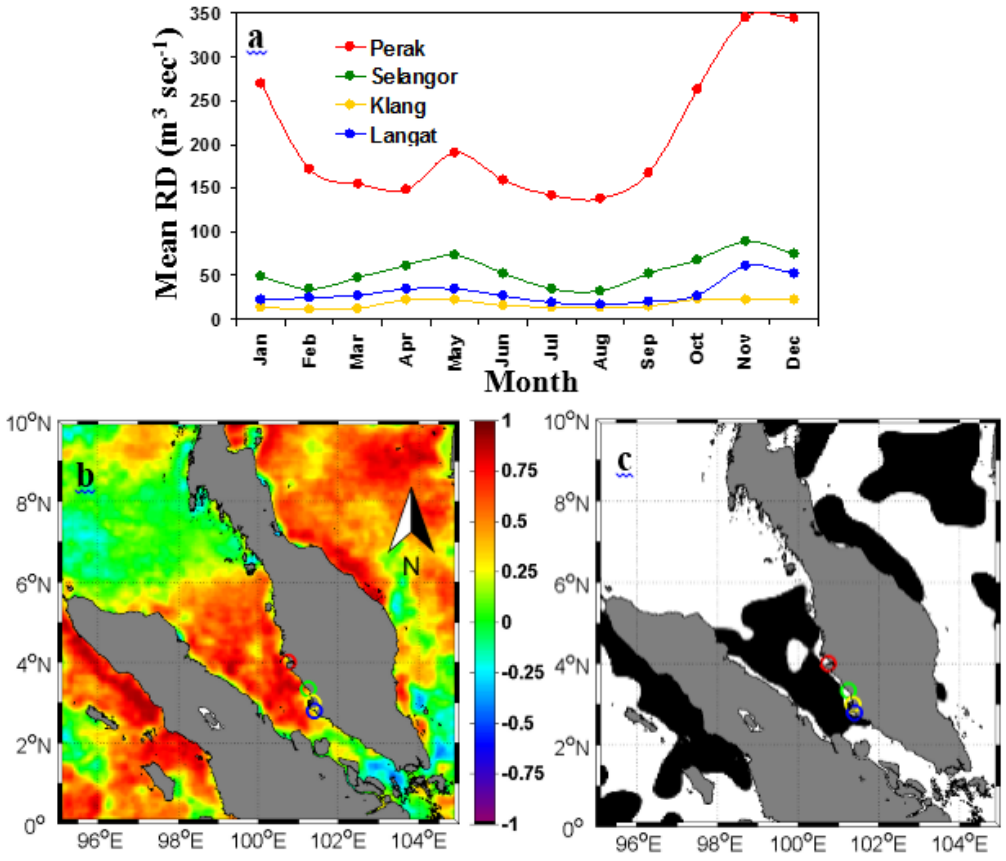

Figure 9. (a) Climatological values of RD into the SM from the Perak, Selangor, Klang, and Langat rivers. Panels (b) and (c) are, respectively, the spatial variation of the correlation coefficient and the corresponding p-value (p) derived from linear regression of monthly climatological SeaWiFS Chl-a on monthly climatological RD averaged for the four main rivers (Perak, Selangor, Klang, and Langat rivers). The black area in panel (c) is the area of correlation coefficient with $p < 0.05$, the indication being that the correlation was significant. Red, green, yellow, and blue circles in (b) and (c) indicate respectively, the estuaries of the Perak, Selangor, Klang, and Langat rivers.

A four-month moving average of Chl-a anomaly (seasonality-removed and detrended Chl-a anomaly) revealed that the largest Chl-a interannual variations occurred in the southern region of the SM, whereas the smallest interannual variations occurred in the northern region (Figure 12a). Interannual Chl-a variations in the southern region were particularly apparent during the period from September 1997 to May 1998 and from July 2004 to March 2007, when Chl-a concentrations tended to be low. The periods from January 1999 to September 2001, from September 2007 to November 2008, and during September 2010, however, were characterized by high Chl-a concentrations.

Interannual variations of Chl-a in the southern region were inversely associated with Nino3.4 (Figure 12a), as is also evidenced by the significant negative correlation between Chl-a anomaly and Nino3.4 (–0.52, $p < 0.01$) (Table 4). This relationship implies that Chl-a in the southern region of the SM tended to be low during El Niño (positive Nino3.4) and high during La Niña (negative Nino3.4) years. In contrast, in the northern region, there was a statistically significant positive correlation (0.26, $p < 0.01$) between Nino3.4 and Chl-a anomaly. There was also a significant positive correlation (0.18, $p < 0.05$) between Chl-a anomaly and DMI in the northern region, but this correlation was weaker than the positive correlation between Chl-a anomaly and Nino3.4. In the middle region, however, there was no apparent association between Chl-a anomaly and Nino3.4 (Figure 12, Table 4), but there was a significant positive correlation (0.31, $p < 0.01$) between Chl-a anomaly and DMI.

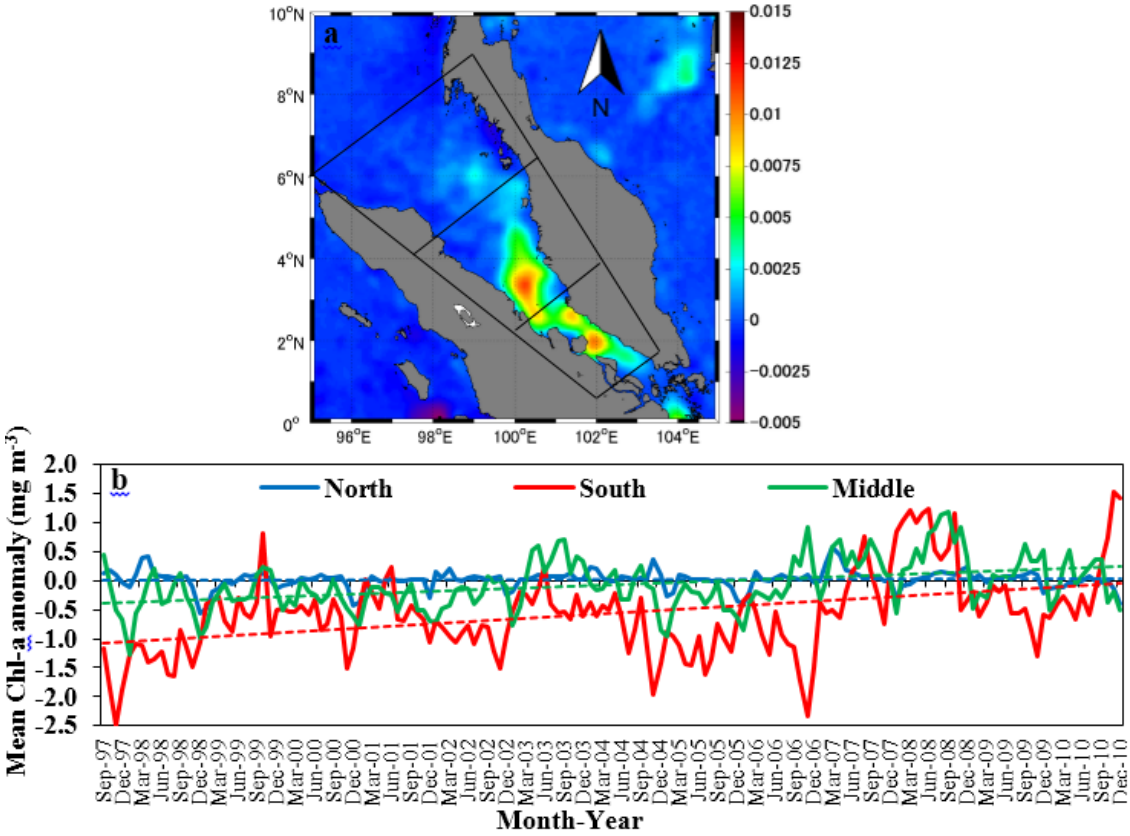

Figure 10. Trends of SeaWiFS Chl-a anomaly (seasonality-removed Chl-a anomalies) during the period of the SeaWiFS full mission depicted as a pixel-based trend map (mg m^{-3} mo^{-1}) (a) and spatially averaged time series (b). Solid lines in (b) are the regression lines that summarize the Chl-a trends for each region. The metrics of the trends are the regression slopes of 0.007, 0.004, and 0.0001 mg m^{-3} mo^{-1} for the southern, middle, and northern regions, respectively.

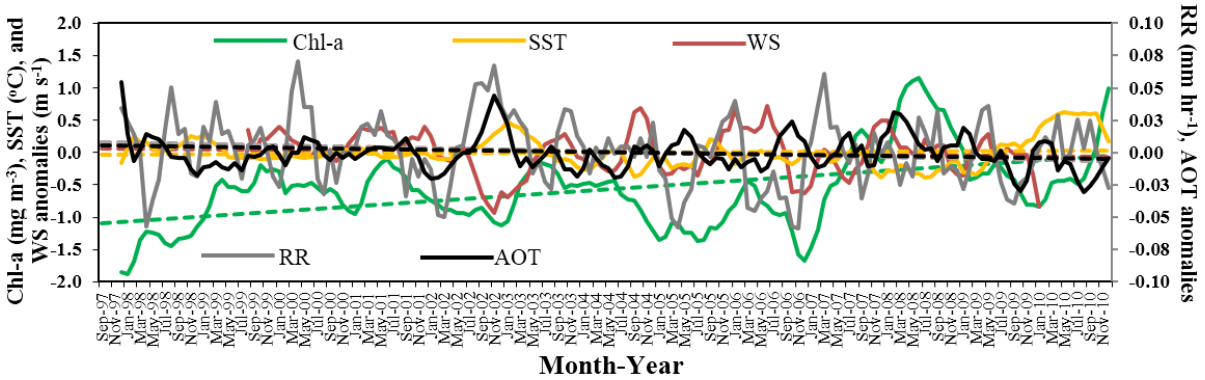

Figure 11. Four-month moving averages of Chl-a, RR, AOT, SST, and WS (seasonality-removed anomalies) in the southern region of the SM during the period of the SeaWiFS full mission. Dashed lines are trend lines derived from linear regressions of variable anomalies versus time (months). The linear regressions for Chl-a, RR, AOT, SST, and WS are associated with correlation coefficients of 0.43 ($p < 0.0001$), 0.07 ($p > 0.3$), 0.12 ($p > 0.1$), 0.05 ($p > 0.5$), and 0.05 ($p > 0.5$), respectively.

Table 4. Correlation coefficients (values between variable anomalies) associated with linear regressions of SeaWiFS Chl-a on DMI, Nino3.4, AOT, RR, U, V, and WS in the northern, middle, and southern regions of the SM. Associations between Chl-a and SST are mentioned here because SST is not the factor that causes temporal variations of Chl-a.

	DMI	Nino3.4	AOT	RR	U	V	WS
North	0.18*	0.26**	0.25*	0.18*	-0.17*	-0.06$^{\#}$	-0.01$^{\#}$
Middle	0.31**	0.15$^{\#}$	0.19*	0.19*	-0.14$^{\#}$	0.16$^{\#}$	-0.10$^{\#}$
South	-0.13$^{\#}$	-0.52**	0.05$^{\#}$	0.17*	0.08$^{\#+}$	-0.05$^{\#+}$	0.16$^{\#+}$

$^{\#}p > 0.05$; *$p < 0.05$; **$p < 0.01$; $^{+}$Wind field data from the middle region of the SM were used.

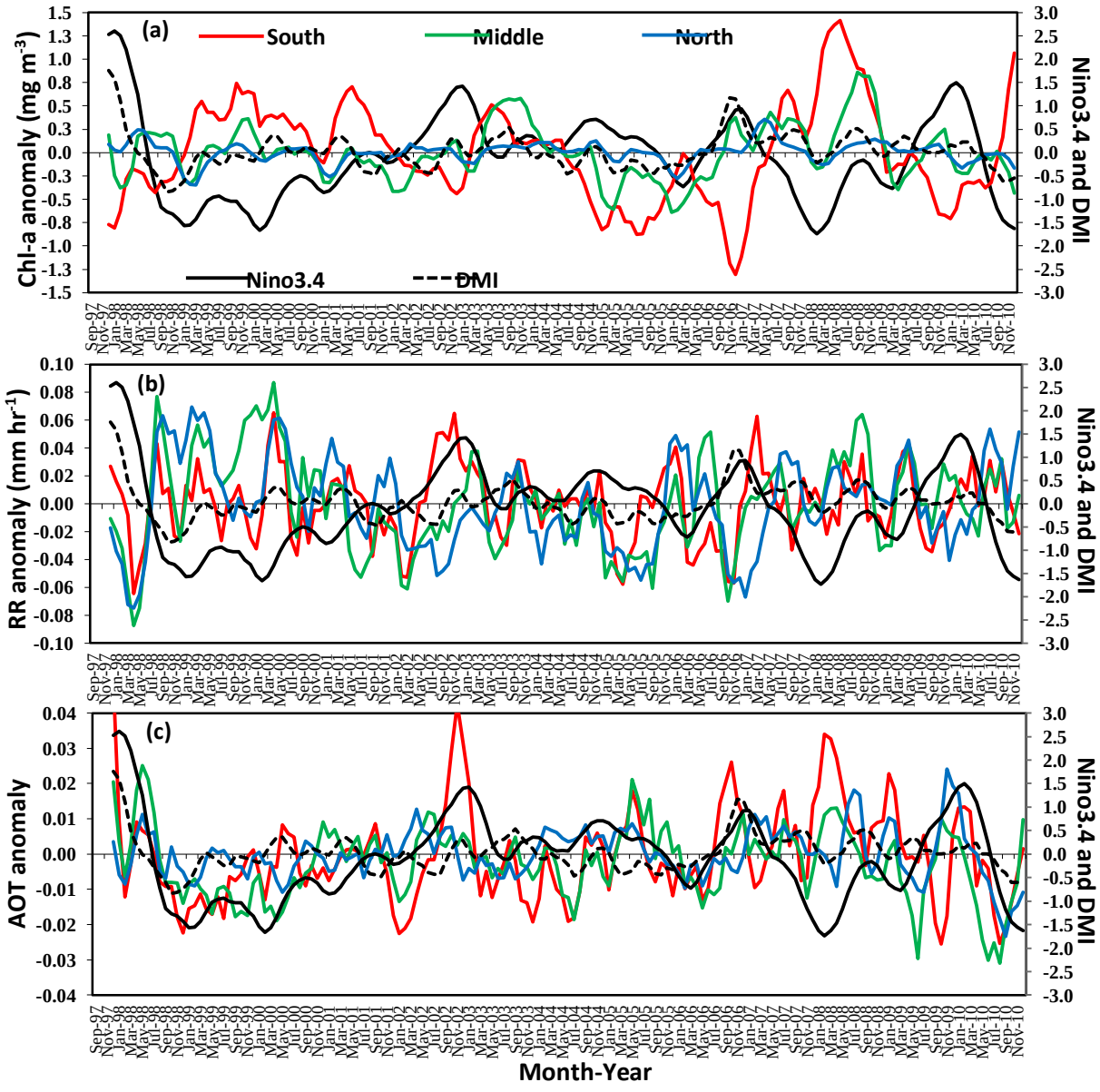

Figure 12. Four-month moving average of SeaWiFS Chl-a anomaly (a), TRMM RR anomaly (b), and SeaWiFS AOT anomaly (c) (seasonality-removed and detrended variable anomalies) in the northern, middle, and southern regions of the SM during the period of the SeaWiFS full mission. Four-month moving averages of Nino3.4 and DMI are also plotted.

In regard to interannual variations, the northern region of the SM seemed to be more responsive to ENSO (0.26, $p < 0.01$) than to IOD (0.18, $p < 0.05$, Table 4). The correlations between positive climate changes and Chl-a increases were nevertheless both statistically significant, the implication being that during both El Niño (positive Nino3.4) and positive IOD events, Chl-a in the northern region tended to increase significantly. Among the investigated environmental variables, AOT is likely the principal factor responsible for interannual variations of Chl-a in the northern region, as evidenced by the significant positive correlation between Chl-a and AOT anomalies (0.25, $p < 0.05$). RR arises as the second most important variable in causing interannual variations of Chl-a in the northern region (0.18, $p < 0.05$ for Chl-a versus RR anomalies). Seemingly, the mechanism by which RR increases Chl-a in the northern region during both El Niño and positive IOD conditions is related to the intensification of wet atmospheric deposition due to high concentrations of atmospheric aerosols during both El Niño and positive IOD conditions.

In the middle region of the SM, Chl-a interannual variations were more responsive to the IOD than to ENSO events. A significant positive correlation (0.31, $p < 0.01$) between the DMI and SeaWiFS Chl-a anomaly in the middle region implies that during positive IOD conditions (positive DMI), Chl-a in the middle region tended to increase. Among the explanatory variables, AOT and RR appear to be the main causes of interannual variations of Chl-a in the middle region, as evidenced by significant correlations between AOT, RR and Chl-a anomalies (0 .19, $p < 0.05$). The same mechanism operative in the northern region also applies in the middle region. Droughts occur during positive IOD event, and both dry and wet atmospheric deposition of aerosols from wildfires likely elevate surface nutrient concentrations.

The climatic anomaly of ENSO seemed to be more important in causing interannual variations of Chl-a in the southern region of the SM (Figure 12a), as evidenced by the significant negative correlation between Nino3.4 and SeaWiFS Chl-a anomaly (–0.52, $p < 0.01$). Among the obvious interannual variations of SeaWiFS Chl-a in the southern region were the low Chl-a concentrations in 1997 and during the period from 2004 to 2006 (Figure 12a, red lines). Those two periods were times of severe drought in Peninsular Malaysia associated with El Niño events. In fact, RR during those periods was anomalously low (Figure 12b, red line). The significant positive correlation (0.17, $p < 0.05$) between SeaWiFS Chl-a and RR anomalies is also noteworthy. This correlation implies that droughts during El Niño events are likely to reduce RR and hence RD, and their reduction further reduces nutrient and sediment loads from the land. This effect will ultimately reduce total suspended matter, both in the form of phytoplankton and inorganic suspended matter, the result being low SeaWiFS Chl-a retrieval in the southern region of the SM during El Niño years. Impacts of large-scale climatic anomalies on seemingly real phytoplankton abundance in the southern region of the SM were hence unresolved in this study, for the reasons described above.

3.1.2. Seasonal Cycle, Interannual Variation, and Decadal Trend of PP in the East China Sea

Seasonal variations of SeaWiFS Chl-a (new product), SeWiFS Kd, and AVHRR SST were remarkable observed as shown in Figure 13. In the coastal region near the Changjiang river mouth, Chl-a was low during winter (January), increase gradually to spring (April), peaked at summer (July) (Figure 13a-d). Such as seasonal Chl-a variation in the ECS is a well-known phenomenon of strong phytoplankton growth dependency on SST (see Gong et al., 2003; Siswanto et al., 2006). As observed by AVHRR, SST was lowest and highest during winter and summer, respectively (Figure 13i-l). During summer, Kd was in the lowest (Figure 13e-h) which was attributed to the low TSM due to summer calm sea surface winds.

The PP estimated by employing PP model and satellite data mentioned above was shown in Figure 14. PP was low during winter (Figure 14a), and reached the highest during summer (Figure 14c). Such a seasonal variation of PP seemed to be caused by a combination of the influences of multi-factors of Chl-a, SST, and Kd. Low PP during winter seemed to be attributed to low SST and high Kd. The high Kd implied that less sunlight would be intercepted by phytoplankton, hence resulting in low

photosynthetic process or low PP. During summer, high SST, high Chl-a, and low Kd seemed to be optimum environmental conditions for the intense growth of phytoplankton, and hence PP in the ECS.

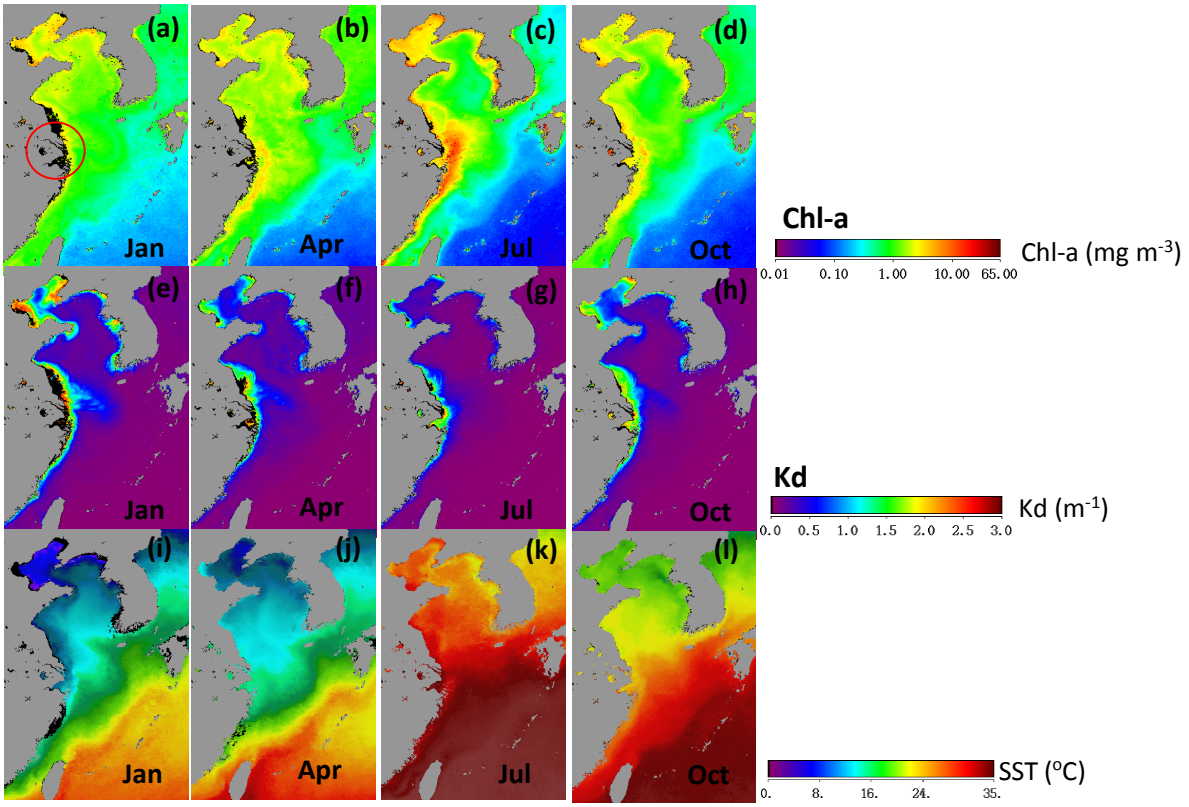

Figure 13. Thirteen-year mean of seasonal variations of SeaWiFS-derived Chl-a (a-d), Kd (e-h), and AVHRR-derived SST (i-l) in the ECS. Red circle in (a) indicates Changjiang estuary.

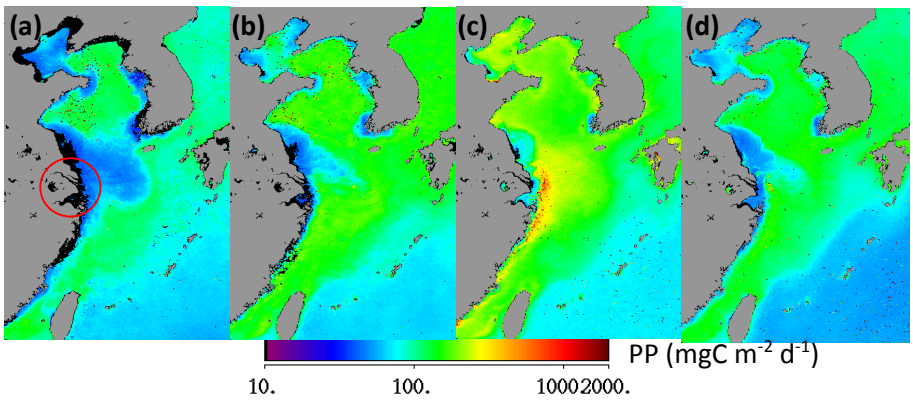

Figure 14. Thirteen-year mean of seasonal variation of satellite-estimated PP in the ECS (a-d). Red circle in (a) indicates Changjiang estuary.

The impact of the world's largest dam, the TGD on PP in the ECS since the first TGD freshwater impoundment (June 2003) has been debated for a long-time. Based on in situ PP data, Gong et al. (2006) mentioned a notable decline of PP during flood seasons between 1998 and 2003. Such a declined PP is believed to be attributed to the decline of nutrients and partly to the invasion of the ECS offshore water due to Changjiang discharge reduction following TGD freshwater impoundment. However, employing high temporal resolution of SeaWiFS chlorophyll-a (Chl-a) data, Yuan et al. (2007)

disputed Gong et al.'s (2006) finding, and claimed that the decline of PP between 1998 and 2003 was more likely attributed to enormous Chl-a interannual variation. It is well known however that, SeaWiFS standard Chl-a used by Yuan et al. (2007) are problematic, especially in the optically complex turbid waters of the ECS where terrestrial origins of colored dissolved organic and total suspended matters are remarkably high (e.g., Siswanto et al., 2011).

Seemingly, the aforementioned dispute stems from the facts that; 1) their arguments on changed PP are based on different variables (i.e., saturated PP in Gong et al. (2006), but Chl-a in Yuan et al. (2007)); 2) low temporal resolution of in situ data used by Gong et al. (2006), hence possibly unable to capture PP interannual variations; and 3) questionable SeaWiFS Chl-a data used by Yuan et al. (2007), though the data had high temporal and spatial resolutions. This chronic problem on the low SeaWiFS Chl-a accuracy, hampered further studies on the PP variation in high spatial and temporal resolutions, though local PP models for the ECS have been earlier developed (e.g., Gong and Liu, 2003; Siswanto et al., 2006). Therefore, in order to provide reliable Chl-a product for the ECS from SeaWiFS radiometric data, Siswanto et al. (2011) developed local Chl-a algorithm based on extensive in situ Chl-a data collected from the ECS and the Yellow Sea.

To be easier to compare to Gong et al.'s (2003), Gong et al.'s (2006), and Yuan et al.'s (2007) results, and to discern interannual PP variation, we remapped Chl-a and PP to cover only the area described in Gong et al.'s (2006). The spatial and seasonal variations of satellite-based Chl-a and PP (Figures 15 and 16) resemble those of in situ Chl-a and PP reported by Gong et al. (2003) suggesting the satellite-based estimations of Chl-a and PP are plausible for discerning PP long-term variation. The notable spatial features of Chl-a and PP are: 1) highest Chl-a and PP are observed during summer especially in the coastal area and areas adjacent to Changjiang estuary; 2) while Chl-a in the Changjiang Bank do not decrease, PP are remarkably low during winter, spring, and fall.

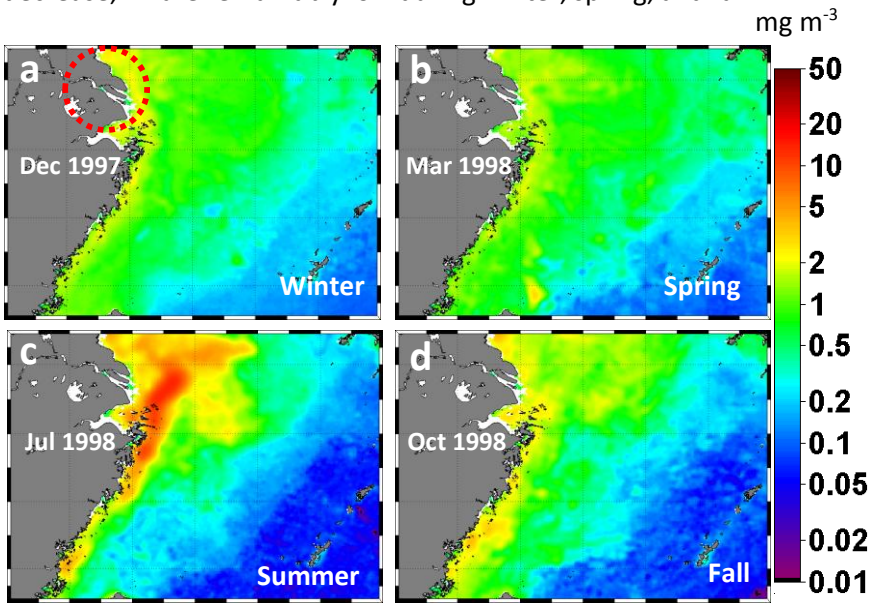

Figure 15. Seasonal variation of satellite-based Chl-a estimated by applying Siswanto et al.'s (2011) local Chl-a algorithm. Data from December 1997 (a), March 1998 (b), July 1998 (c), and October 1998 (d) representing respectively, for winter, spring, summer, and fall periods were selected here to be compared with Gong et al.'s (2003) results (see their Figure 8). Red dotted circle in (a) indicates Changjiang estuary.

In order to understand the possibility of the TGD fresh water impoundment in June 2003 and its modified Changjiang RD and CDW, we derived time series of PP only over the CDW the water with SSS < 32 (e.g., Siswanto et al., 2008). The area of CDW was at the largest during summer (Figure 17c) due to the highest Changjiang RD (Figure 18a). Our satellite-based PP time series shows that there was a declined PP in the area adjacent to Changjiang estuary during 2003 flood season (June ~ August),

compared to that during 1998 flood season, which is consistent with Gong et al.'s (2006) result. However, low PP during flood season were also observed in the other years without TGD freshwater impoundment. PPs during 2004 flood season were also higher than those during 2003 flood season (called as moderate PP recovery in Gong et al. (2006)).

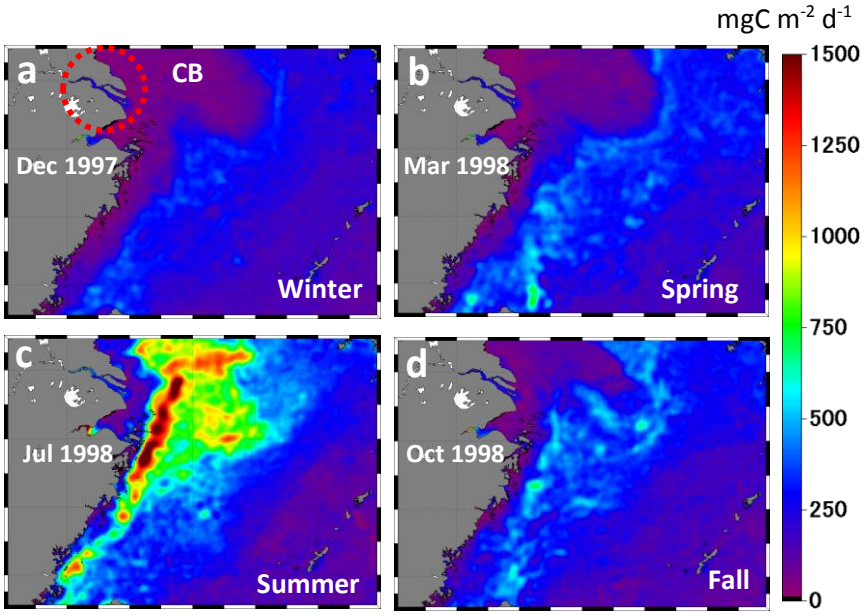

Figure 16. Seasonal variation of satellite-based PP estimated by applying Gong and Liu's (2003) local PP model and Siswanto et al.'s (2011) local Chl-a algorithm. See Figure 9 in Gong et al.'s (2003) for comparison. Red dotted circle and CB in (a) indicates Changjiang estuary and Changjiang Bank, respectively.

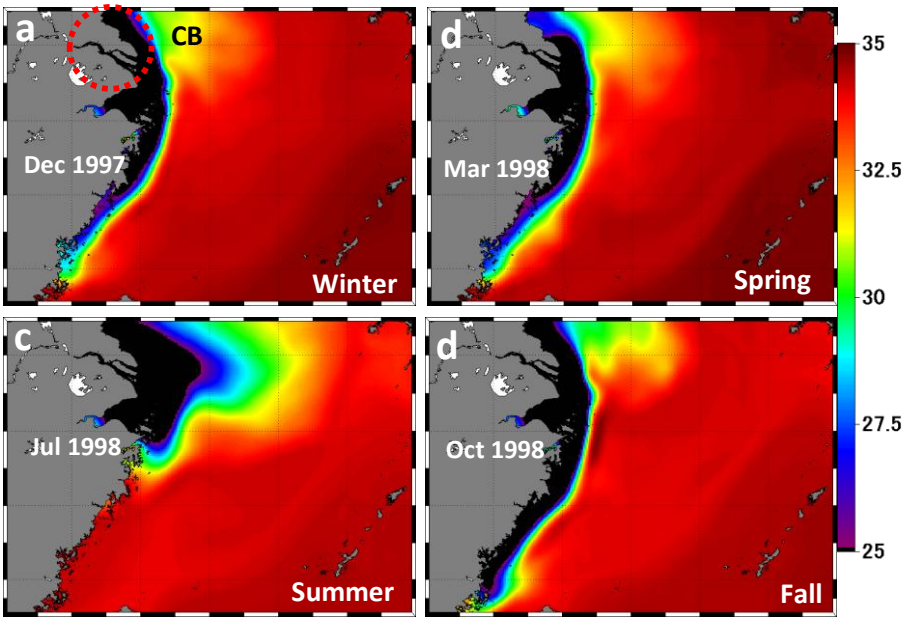

Figure 17. Seasonal variation of SSS from FRA-JCOPE2. Red dotted circle and CB in (a) indicates Changjiang estuary and Changjiang Bank, respectively.

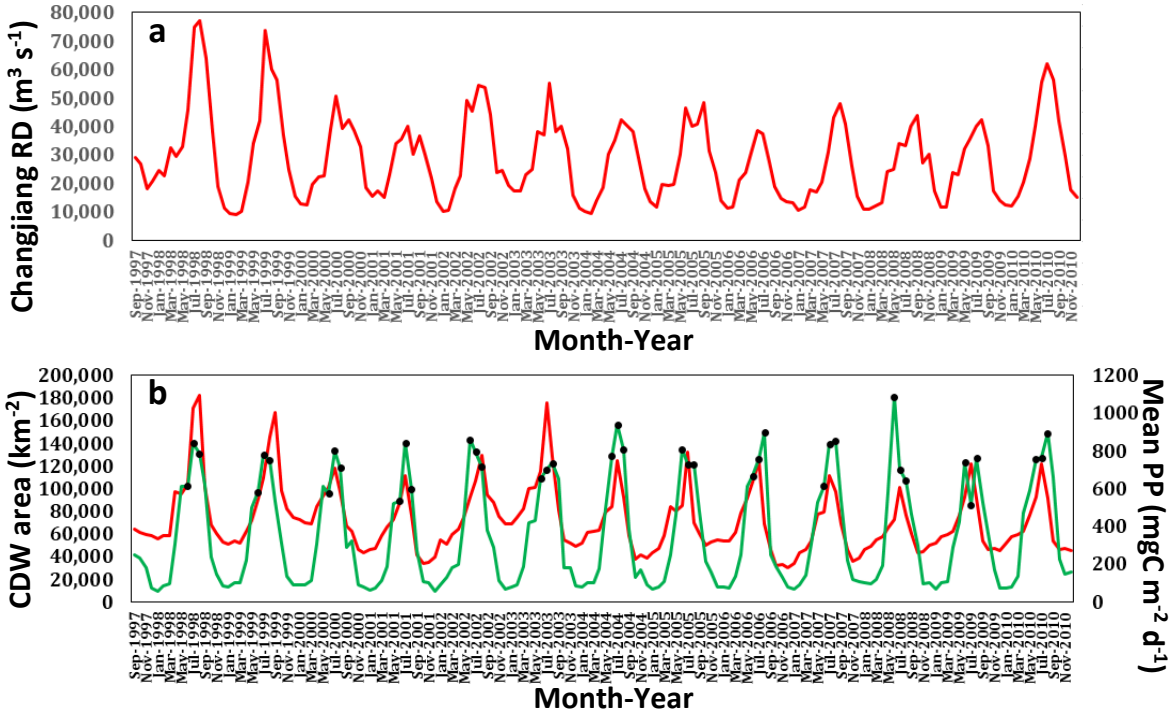

Figure 18. Time series of satellite-based PP (green line) within the period of SeaWiFS full mission (September 1997 ~ December 2010) averaged over the CDW area. Time series of CDW area (red line) is also mentioned. Three black dotted data in each year indicate the data during the flood season (July ~ September).

Observing PP during flood season from the other years, PP in this area shows high interannual variation, hence in agreement with Yuan et al.'s (2007) postulate. Anomalously high PP was observed in June 2008 (Figure 18b), but both Changjiang RD and CDW area showed no anomalous conditions (Figure 18a and b). Seemingly, the anomalous PP in June 2008 was more associated with massive red tide at the coastal area of China (see Figure 19a). The impact of TGD freshwater impoundment to decrease PP inferred from the declined PP between July 1998 and June 2003 (Gong et al., 2006) may hence need to be reconsidered at least for the reasons that 1) annually, July is the period of highest PP, hence by average June PP is normally lower than July PP, 2) high PP in July 1998 is probably highly influenced by catastrophic summer flood in Changjiang basin associated with 1997/1998 ENSO event, 3) low PPs during flood season were also observed in the years without freshwater impoundment between 1998 and 2003, and 4) high PP since 2003 are frequently observed which may be associated with more frequent red tide events in the areas adjacent to Changjiang estuary.

In terms of long-term PP trend, the analysis found that PP tended to decrease in the region adjacent to the Changjiang estuary (Figure 20a). The decreasing trend seemed to be more remarkable during flood season (Figure 20c) when the Changjiang RD reaches its highest. In contrast, at the same area, TSM tended to decrease both especially during flood season (Figure 20b,d). The fact that PP near Changjiang estuary is largely controlled by TSM (e.g., Gong et al., 2003), the decreased TSM in the area adjacent to Changjiang estuary seemed likely to improve water column light quality, leading to increased phytoplankton growth, manifested as increased PP. However, further study is needed to clarify whether TSM is the only driving variable, or other variables of Changjiang RD, CDW area, and other physical oceanic variables may also drive the observed PP increasing trend.

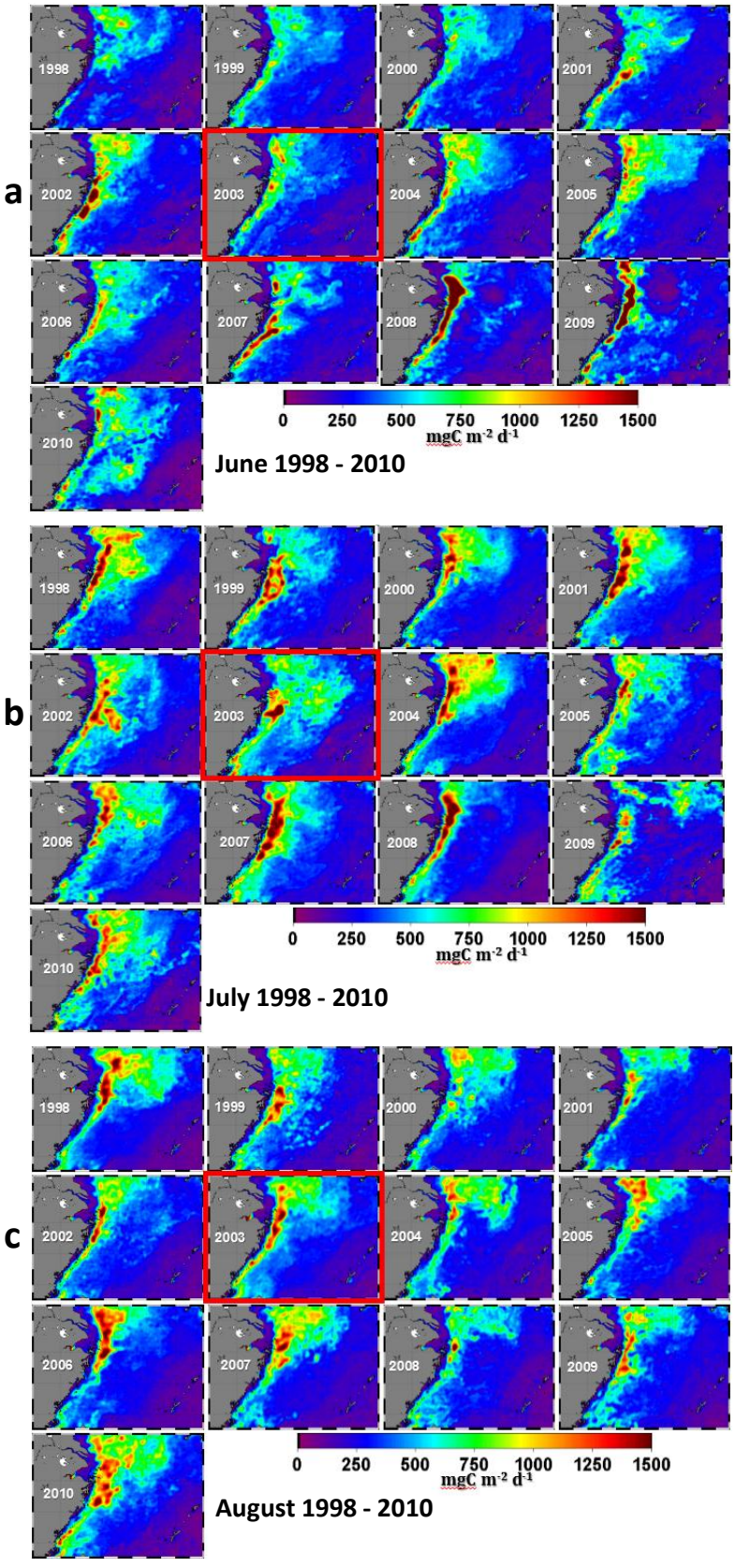

Figure 19. Satellite-derived PP for June (a), July (b), and August (c) the years from 1998 to 2010. Red box for 2003 indicates the year of the first TGD freshwater impoundment, started in June 2003. June, July, and August PP images are mentioned here, as those period is the period of flood season.

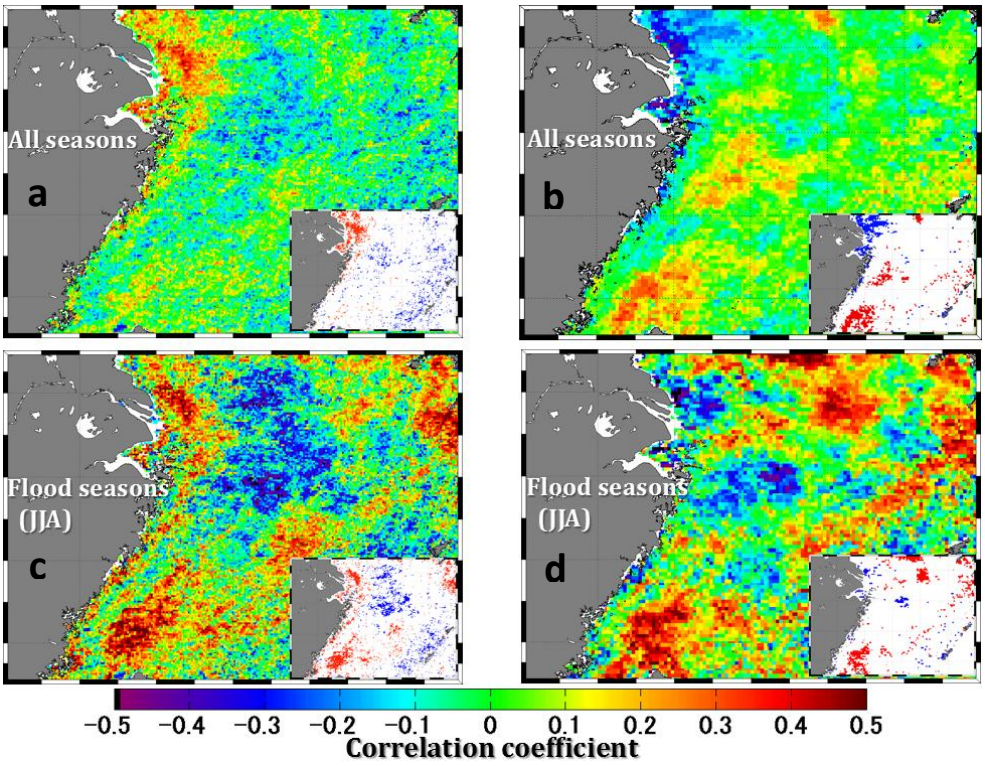

Figure 20. (a) and (b) are maps of correlation coefficients between PP and time (month) for all seasons (a) and for flood season only (June ~ August, c), respectively. (b) and (d) are same as (a) and (c), except between TSM and time. Smaller map shows the areas only with significant ($p<0.05$) negative correlation (blue) and significant positive correlation (red), which can be indicatives of remarkable decreasing trend and increasing trend, respectively.

3.1.3. Seasonal Cycle and Interannual Variation of Chl-a in the South China Sea

Unlike in the ECS, Chl-a in the SCS both in the coastal and offshore regions were relatively higher during winter (Figure 21l) than during other seasons. Chl-a was in the low level during the period from April to June (Figure 21d-21g). During summer, Chl-a enhancement was observed along the coast of Vietnam and extended to the middle/offshore region of the SCS (Figure 21g-21i). This coastal Chl-a enhancement was associated with summer coastal upwelling driven by prevailing along shore southerly wind (Zhao and Tang, 2007) (see also Figure 22f-h). In winter on the other hand, another Chl-a enhancement was observed northwest of Luzon Island, Philippines. This Chl-a enhancement started to develop from November and lasted till March (Figure 21a,b,c,k,l). During this period, winds over the SCS blew from north to south to induce winter upwelling (Figure 22k,l,a). Upwelling occurred along the coast of Vietnam during summer and northwest of Luzon Island during winter brought nutrient-rich deep water to the surface layer. Nutrients in the surface layer were then replenished, which in turn would be available for phytoplankton growth resulting in high Chl-a.

As an initial attempt to understand the impact of global climate change on the Chl-a variation in the SCS, we plotted the 13-year SeaWiFS Chl-a averaged over the entire region of the SCS superimposed on Nino 3.4 index to represent ENSO event (Figure 23). It was observed that Chl-a in the SCS tended to decrease during El Nino years, but increase during La Nina years. The impact of ENSO on Chl-a variation in the SCS was already known from previous studies (e.g., Zhao and Tang, 2007). However, which part of the SCS was more vulnerable to El Nino and La Nina, which environmental factors co-varied with ENSO and probably determine interannual variation of Chl-a

associated with climate change, and whether ENSO influences Chl-a variation in the same time frame (no time-lag), are less documented.

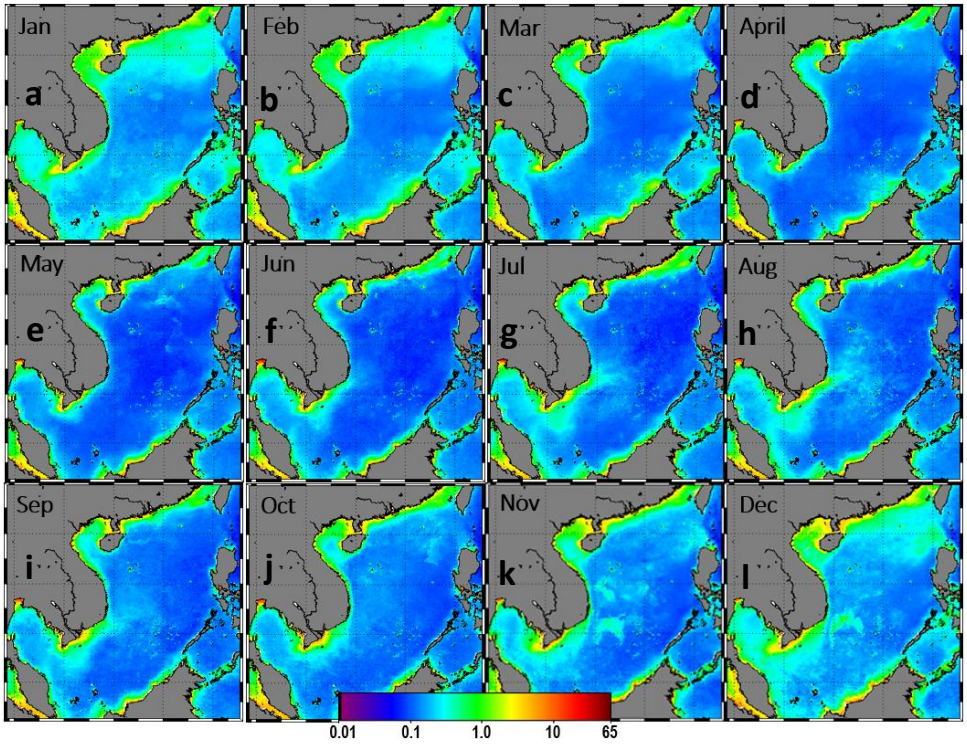

Figure 21. Monthly climatological means of SeaWiFS Chl-*a* (mg m^{-3}) averaged from monthly SeaWiFS Chl-*a* data (September 1997 to December 2010).

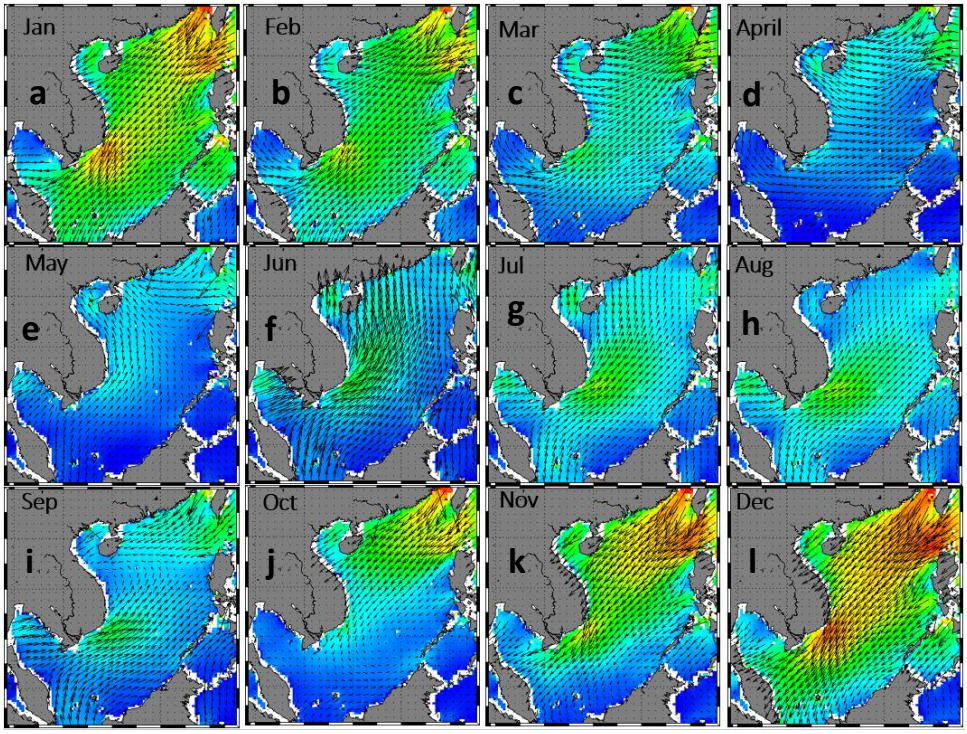

Figure 22. Monthly climatological means of QuikScat wind field (mg m^{-3}) averaged from monthly QuikScat wind field (September 1997 to December 2010). Color scale and arrow indicate wind speed magnitude and wind direction.

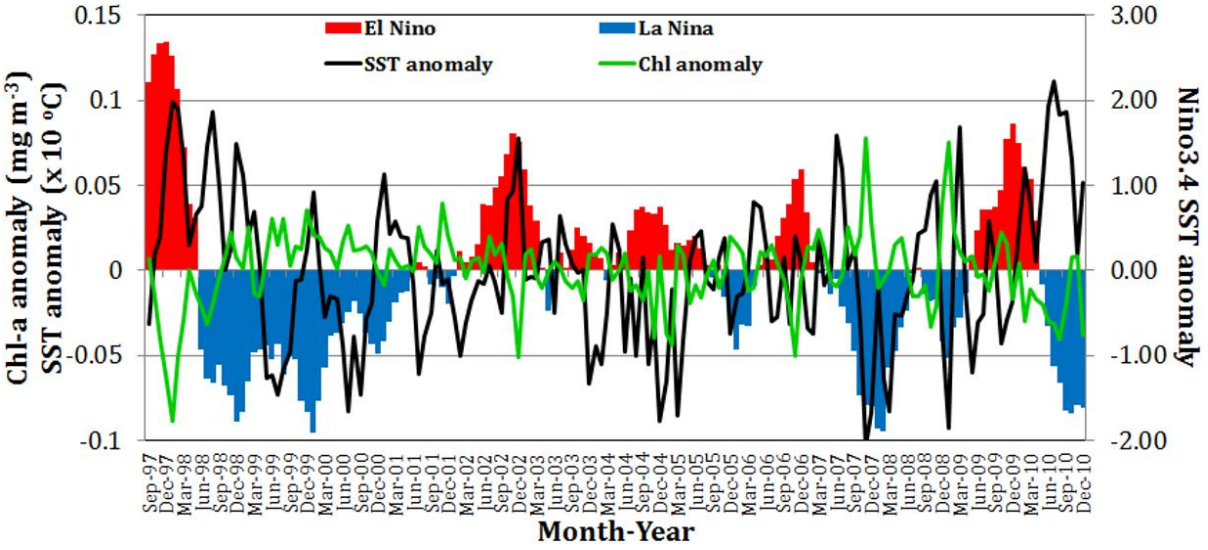

Figure 23. Time series of SeaWiFS Chl-a (green line) and AVHRR/MODIS SST (black line) within the period of SeaWiFS full mission (September 1997 ~ December 2010) averaged over the entire region of the ECS. Time series of Nino3.4 index (red/blue bar) is also mentioned.

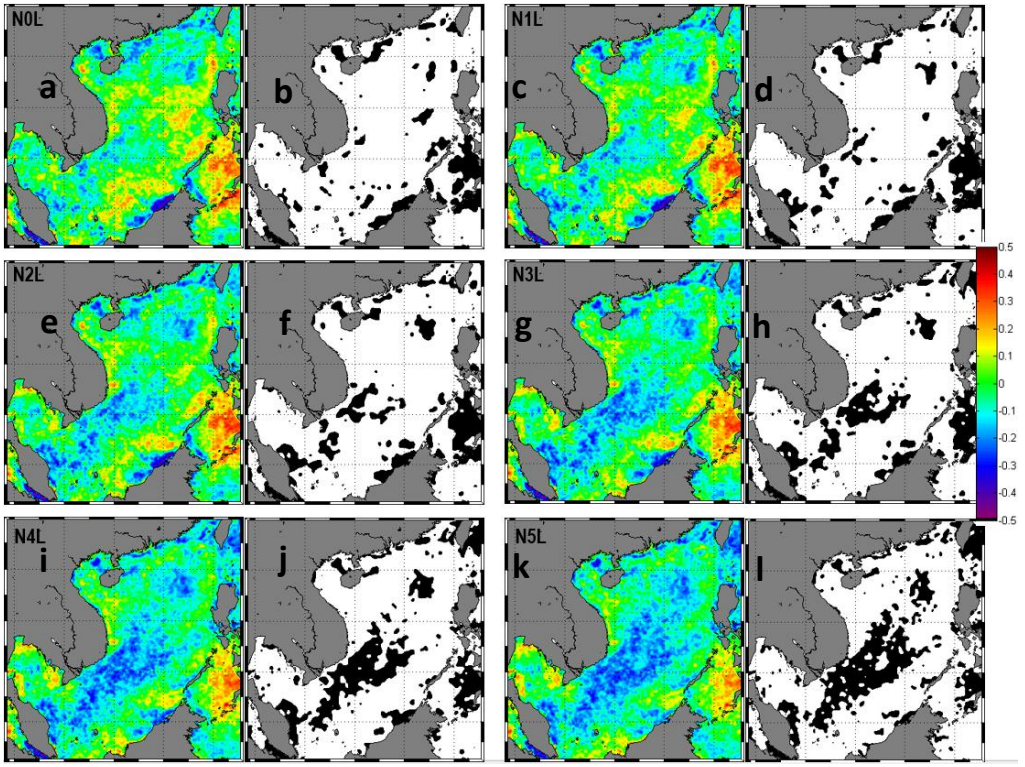

Figure 24. Maps of correlation coefficient between SeaWiFS Chl-a anomaly and Nino3.4 index. NXL (where X = 0-5) indicates time lag (in month) between Nino3.4 and Chl-a time series. For instance, N1L means Nino3.4 time series lead Chl-a time series by one month. Black and white maps on the right column indicate the map of significant correlation, where black area indicates the regions with significant negative/positive correlation.

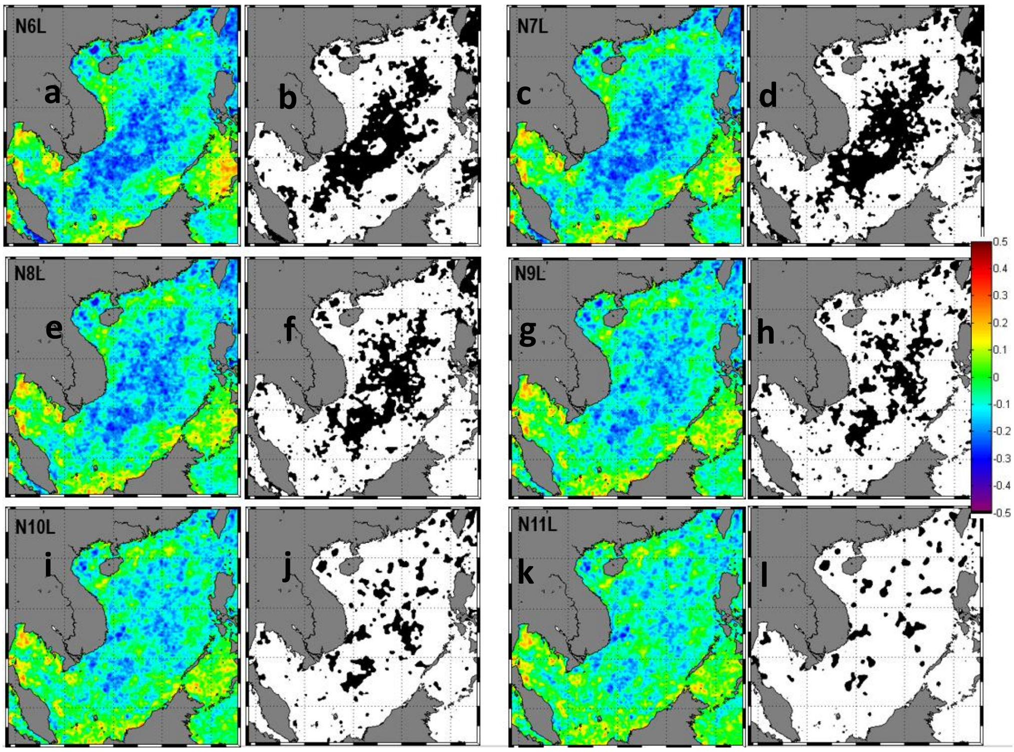

Figure 25. Same as Figure 24, except for X = 6-11 (from 6-month to 11-month time lags).

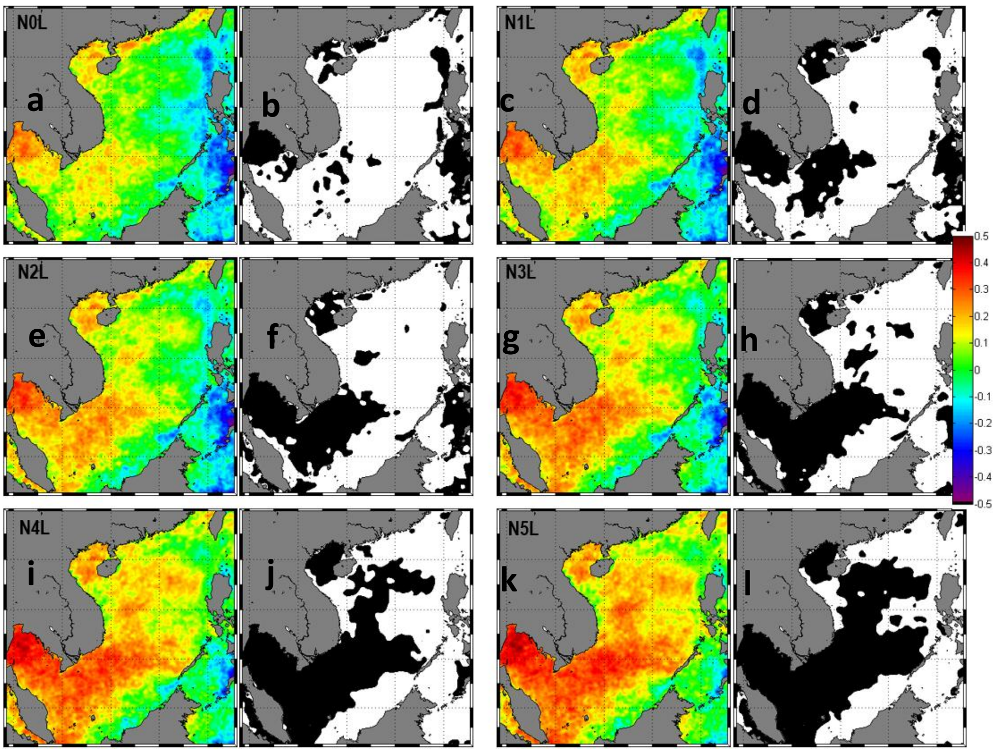

Figure 26. Maps of correlation coefficient between AVHRR/MODIS SST anomaly and Nino3.4 index. NXL (where X = 0-5) indicates time lag (in month) between Nino3.4 and Chl-a time series. For instance, N1L means Nino3.4 time series lead Chl-a time series by one month. Black and white maps on the right column indicate the map of significant correlation, where black area indicates the regions with significant negative/positive correlation.

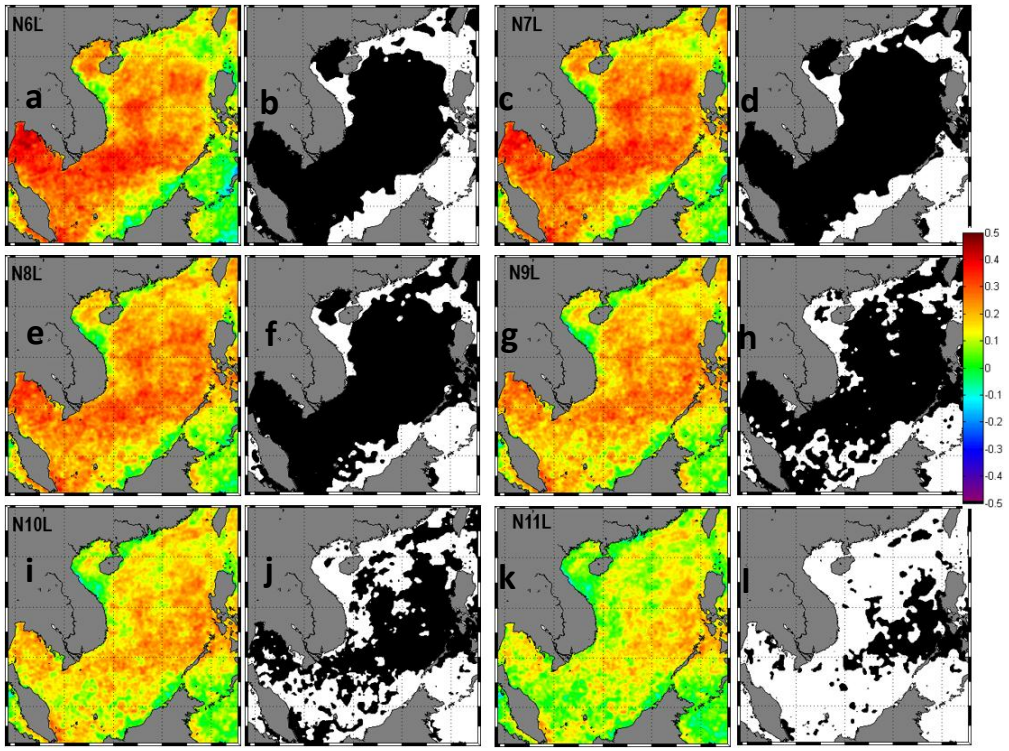

Figure 27. Same as Figure 26, except for X = 6-11 (from 6-month to 11-month time lags).

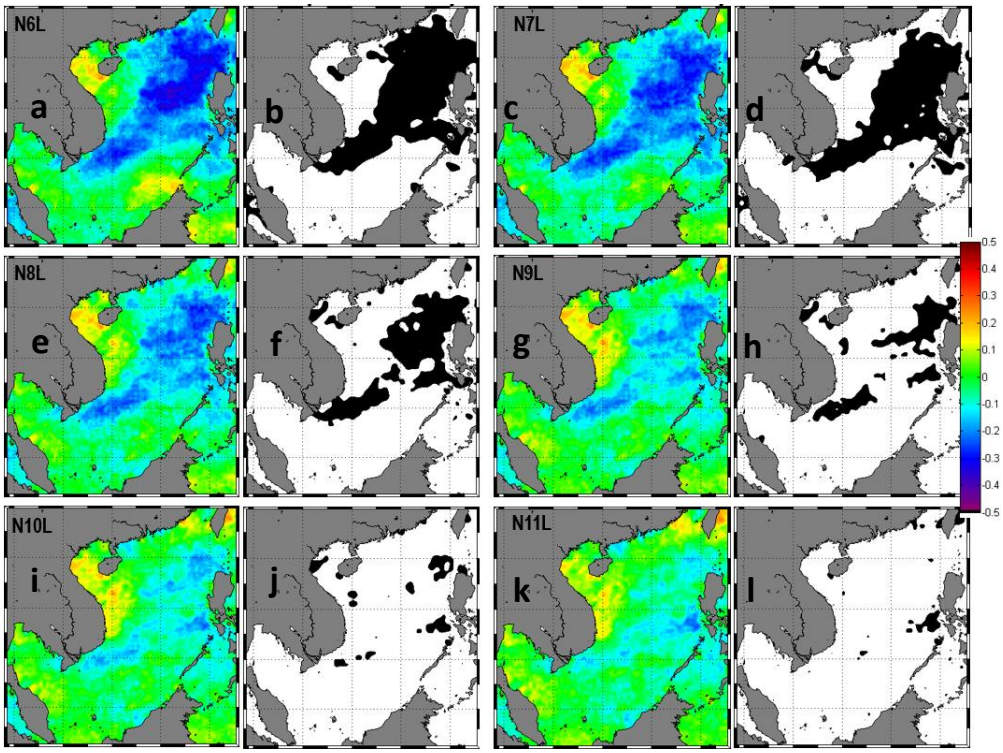

Figure 28. Maps of correlation coefficient between QuikScat WS anomaly and Nino3.4 index. NXL (where X = 0-5) indicates time lag (in month) between Nino3.4 and Chl-a time series. For instance, N1L means Nino3.4 time series lead Chl-a time series by one month. Black and white maps on the right column indicate the map of significant correlation, where black area indicates the regions with significant negative/positive correlation.

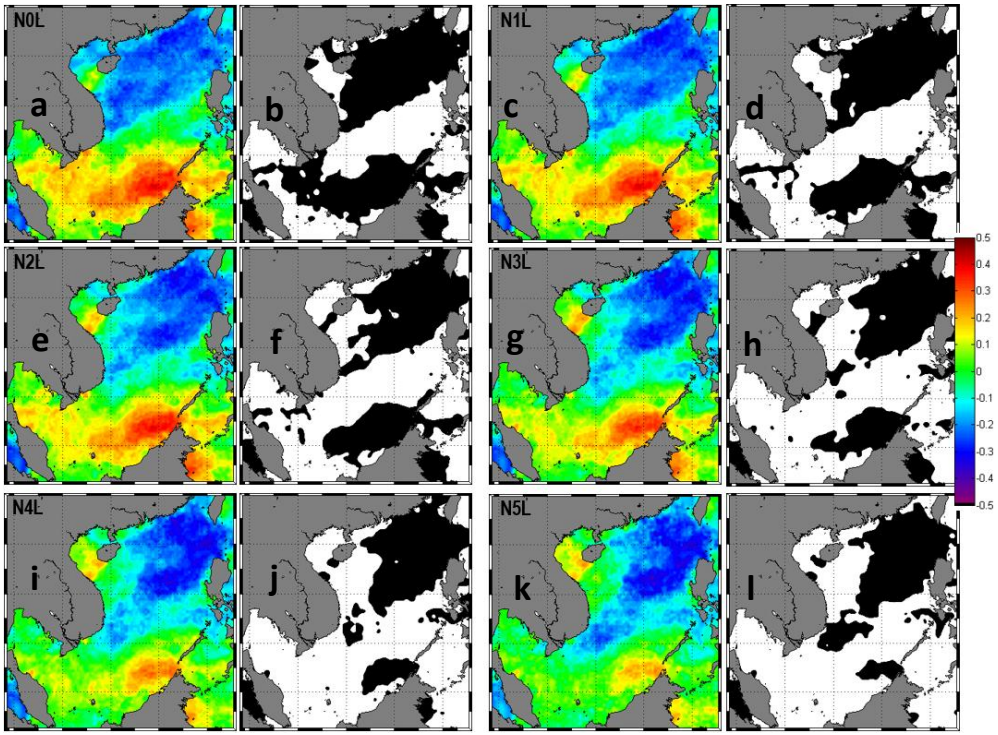

Figure 29. Same as Figure 28, except for X = 6-11 (from 6-month to 11-month time lags).

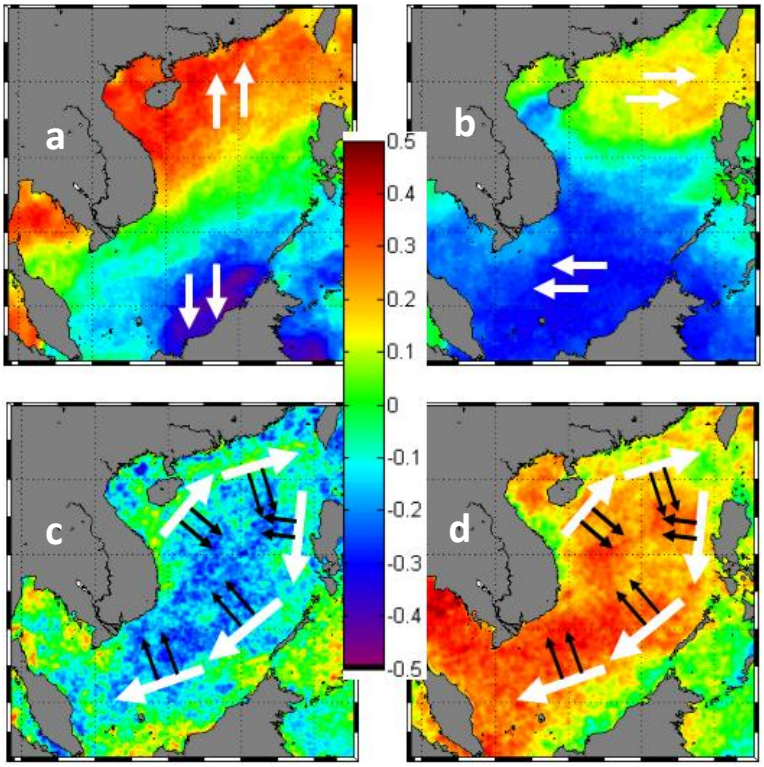

Figure 30. Spatial variation of correlation coefficients between Nino3.4 index and variable anomalies of QuikScat meridional wind component (a), QuikScat zonal wind component (b), SeaWiFS Chl-a (c), and AVHRR/MODIS SST (d). Correlation coefficient here was derived with 6-month El Nino leading. White arrows indicate tendency of anomalous wind direction/circulation. Black arrows indicate the direction of Ekman transport resulted by anti-cyclonic anomalous wind circulation (white arrows in (c) and (d)).

In contrast to Chl-a, satellite SST tended to be high during El Nino, and low during La Nina (Figure 23). Increasing SST during El Nino implies that El Nino seemed to reduce vertical entrainment of cold deep water to the surface (sun lit) layer. This also implies that vertical entrainment of nutrient weakened, which reduced nutrient availability for phytoplankton growth in the surface layer, and eventually manifested as decreased Chl-a during El Nino. Zhao and Tang (2007) mentioned that El Nino decreased Chl-a only in the limited area west of Vietnam which was considered to be due to weakened summer upwelling caused by weakened southwesterly SWM winds. To discern the spatial extent of the impact of ENSO on Chl-a variability, we derived Chl-a anomaly and correlation coefficient between Chl-a anomaly and Nino3.4 index.

Spatial and temporal variation analysis on the Chl-a anomaly and Nino3.4 index correlation coefficient revealed that there was an evolution on the association between Chl-a and El Nino. At 0-time lag, there was still no influence of ENSO on Chl-a variation in the ECS. El Nino seemingly started to decrease Chl-a initially in the area west of Vietnam within 2-month after the El Nino onset (Figure 24). Since then, the area of declined Chl-a expanded with time. Six months following El Nino signal, the area showing declined Chl-a reached the largest, and maintained at least 9 month following El Nino signal (Figure 25). The possible factor of decreasing nutrient entrainment from deep layer to sun lit layer during El Nino as briefly described above was also clearly observed by the same time-lag of the response of increasing SST to El Nino as that of declining Chl-a to El Nino. At 0-time lag, almost no response of SST to El Nino (Figure 26), but 6 months after El Nino signal, SST seemed to increase almost over the entire SCS (Figure 27). Such a large area of increased SST maintained to at the latest 9 months following the El Nino signal (Figure 27).

Consistent with Zhao and Tang (2007), during El Nino, weakened WS during El Nino was also observed from our analysis. The weakened WS west of Vietnam coast also started to 2 months after the El Nino signal, and the area of weakened WS expanded and was still observed 9 months following the El Nino signal (Figures 28 and 29). However, the declined Chl-a was not only observed in the area west of Vietnam coast, but also over a large area in the center of the SCS elongated from southwest to northeast direction. Analyzing wind components, we found that during El Nino, meridional winds in the north region of the SCS tend to be positive (stronger northward winds), but in the south region of the SCS, tend to be negative (stronger southward winds) (Figure 30a). In terms of zonal winds, we found that, in the north region of the SCS, zonal winds tend to be positive (stronger eastward winds), but in the south region, tend to be negative (stronger westward winds) (Figure 30b).

The anomalous wind components during El Nino (Figure 30a,b) led to anomalous anti-cyclonic wind circulation as depicted in Figure 30c,d. Such an anti-cyclonic wind circulation eventually led to Ekman transport to be directed to the center of the SCS, hence to favor downwelling condition in the SCS during El Nino. This anomalous downwelling condition is then the mechanism underlying the declined SeaWiFS Chl-a and increased AVHRR/SST during El Nino event (Figure 30c,d).

3.2. Numerical Modeling for Researches in the Gulf of Thailand and the South China Sea

3.2.1. Circulation in the South China Sea

Current patterns change seasonally (Figure 31) following seasonal winds (Figure 22). Monthly averaged circulation patterns are presented and discussed. During the NEM (January), surface currents along southern China and Vietnamese coast direct westward and southward, respectively. Strong surface currents are observed near the Mekong River mouth. Some part of these currents move into the central GoT during this time. Overall circulations in the SCS seem to direct counter-clockwise with inward currents through the northern and the eastern channels and outward currents through the southern channel. Currents in deeper layer (100 m) also tend to flow counter-clockwise along the SCS deep basin. The directions of surface currents during the SWM reverse from those during the NEM. Most currents direct northward from the southern to the northern channels. Surface currents in the GoT flow outward mostly along the western coast into the SCS where the northeastward currents near the gulf mouth locate. However, there are some currents flow southward along the Vietnamese coast started from the central Vietnam to the northern area of the Mekong River mouth.

This southward currents then diverge with the northward currents flowing from the southern Vietnamese coast and move southeastwardly offshore after that. Currents in deeper layer still direct counter-clockwise along the deep basin in the same way as those during the NEM. Just a meander in the central basin that changes the directions form southwestward to northeastward.

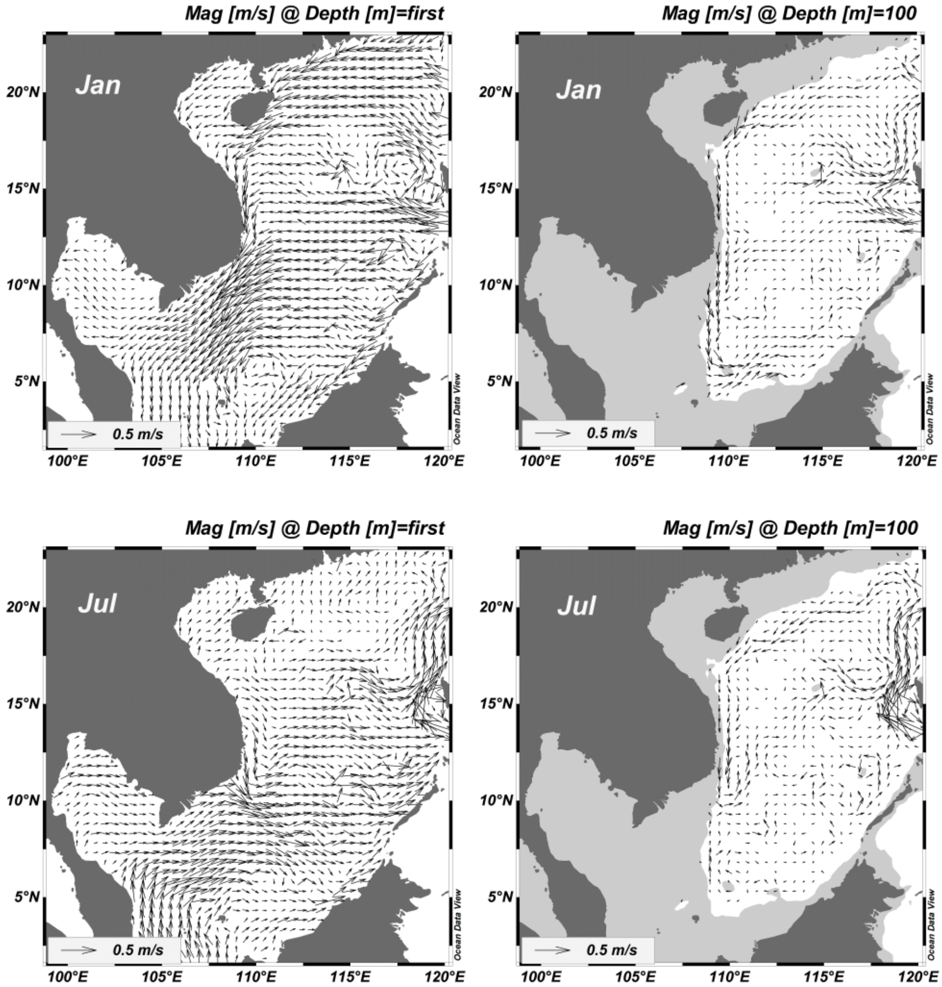

Figure 31. Horizontal circulations at the sea surface and at 100 m depth during the NEM (January) and the SWM (July).

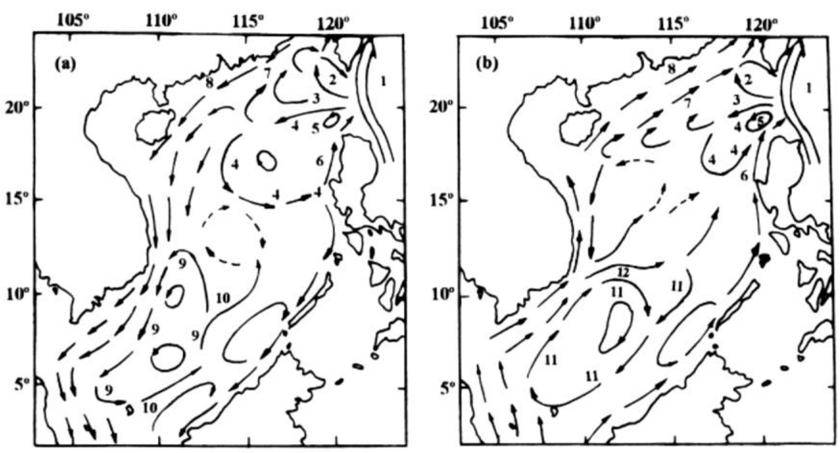

Figure 32. schematic of surface circulation in the South China Sea in (a) winter and (b) summer. (Fang et al., 1998).

Compared to the surface circulation patterns summarized in Fang et al. (1998) (Figure 32), the results from our study mostly agree with them that the southward and the northward flows along the southern China and Vietnamese coast develop during the NEM and SWM, respectively. Flows in the western areas along the Indonesia and the Philippines archipelagoes also agree well that the southward and the northward flows develop during the NEM and SWM, respectively. Discrepancies between the results from this study and the previous one are found in the central SCS and along the central Vietnamese coast during the SWM. Circulations in the central SCS in both seasons from this study seem to be not complex like the schematic diagram of circulation patterns in the previous report. For the central Vietnamese coast, both results agree that southward flows during the SWM occur there but the position of the offshore meander in the previous report locates further in the north and direct eastward instead of southeastward in the same way as in the results of the present study.

Disagreement between the results may be related to modeling techniques including wind forcing and boundary conditions. This experiment uses monthly wind in January and July to represent the NEM and SWM, respectively. It is possible that the wind patterns of selected months are somehow different from the seasonal wind. When the wind patterns are different, the circulation patterns are also different. Boundary condition may be another source of error. This numerical experiment lacks of the information of flows through channels surrounding the SCS. Therefore they were set to no flow condition, and just let tide in terms of water elevation influences circulation in the computational area with other forces. Such external flows may play an important role to the current patterns in the SCS.

As a 3-dimensinal ocean model, POM can be used to investigate upwelling and downwelling in the SCS as shown in Figure 33. These vertical flows are clearly observed in the west and the east of the deep SCS basin. Downwelling area lining from the central Vietnamese coast southwardly down to around latitude 5^{o}N while upwelling occurs along the Indonesia and the Philippines archipelagoes during the NEM. These can be explained by the development of surface convergence and divergence. Downwelling near the west coast is generated by convergence of strong currents near the Mekong River mouth following wind direction. Upwelling along the eastern islands is induced by divergence generated by offshore surface flows (Figure 31). In contrast, strong upwelling and downwelling develop during the SWM in the same downwelling and upwelling area, respectively, during the NEM. Reversing wind and current directions play significant roles to these phenomena. The development of divergence in the west of the basin near the southern west coast is due to offshore surface flow during this time. Downwelling in the east SCS is explain by coastal convergence generated by flow into the western islands.

The development of upwelling in the southern Vietnamese coast during the SWM somewhat agree to high chlorophyll-a concentration derived by satellite images in almost the same area reported by Tang et al. (2006). The upwelling area developed by this numerical experiment however is located further in the south and offshore when compared to satellite imageries in the previous study. This is due to the development of divergence zone related to surface circulation and wind. Variations in these environmental factors may be responsible for this discrepancy.

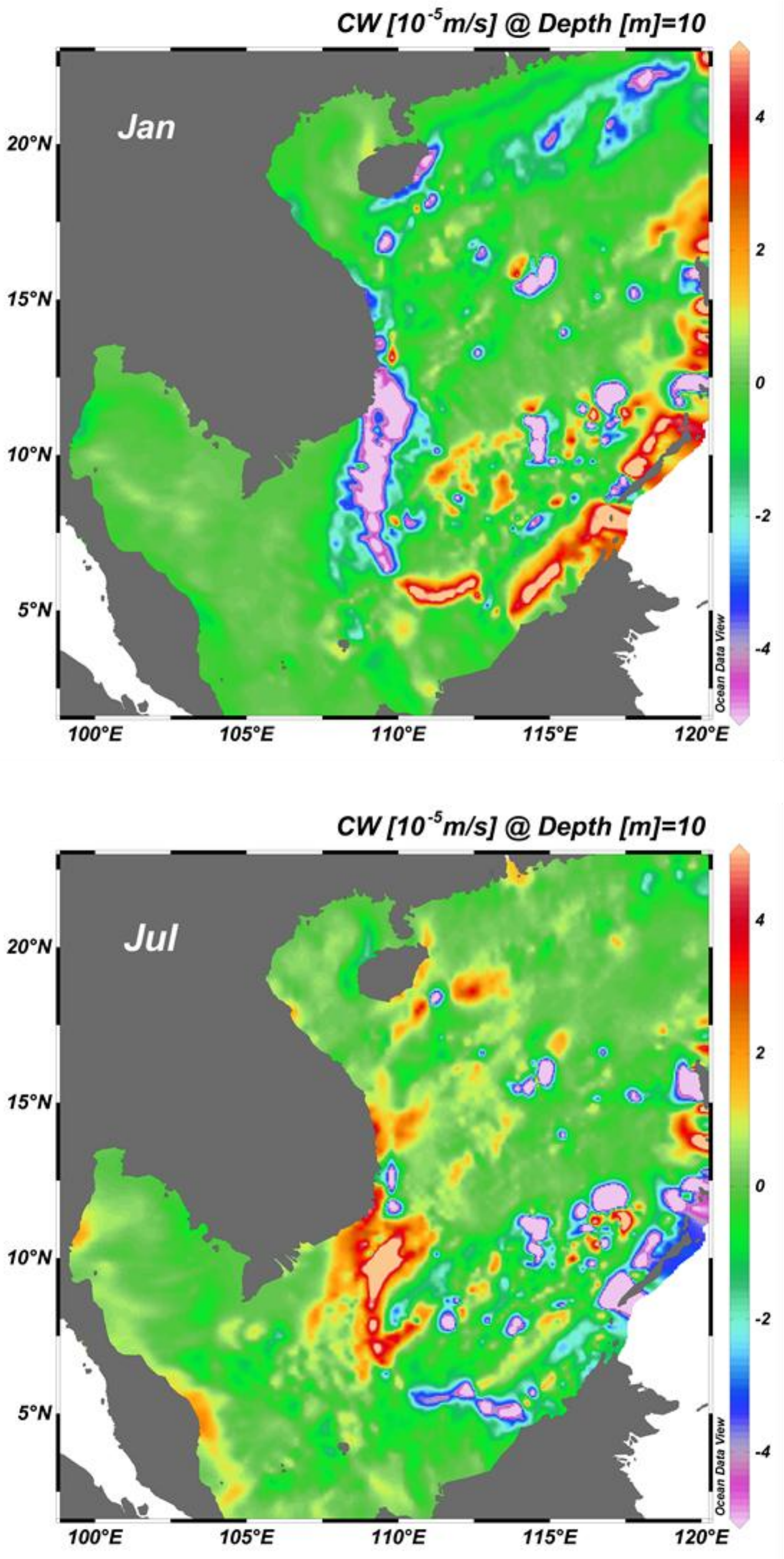

Figure 33. Horizontal distributions of vertical velocities during the NEM (January) and the SWM (July).

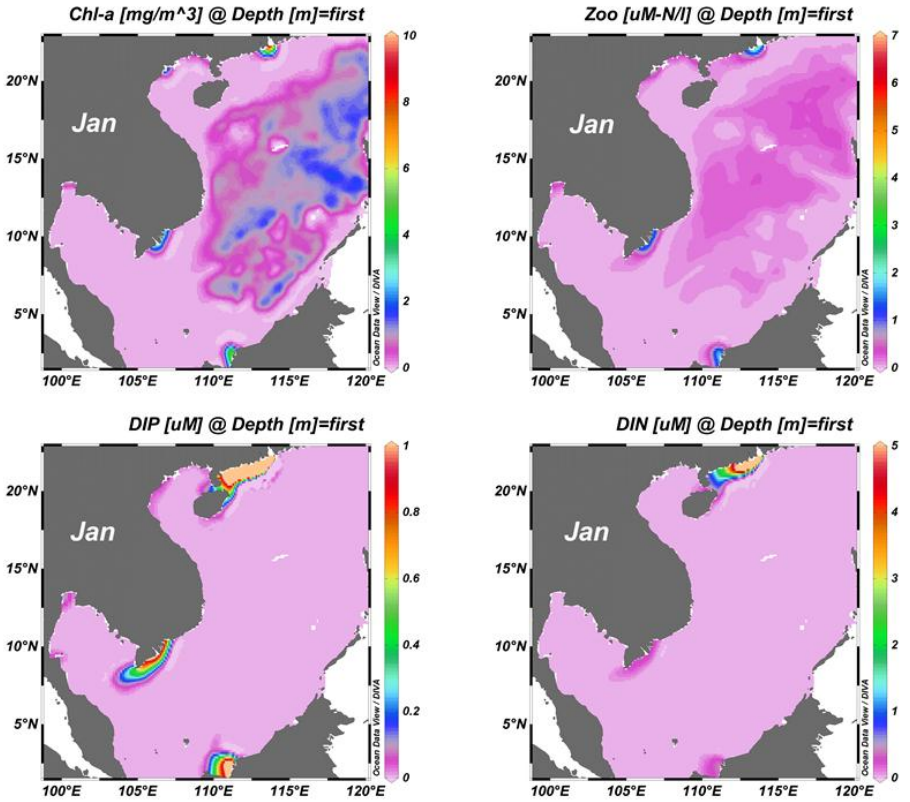

Figure 34. Horizontal distributions of Surface chlorophyll-a, Zooplankton, DIP and DIN during the NEM (January) simulated using POM-NPZD model.

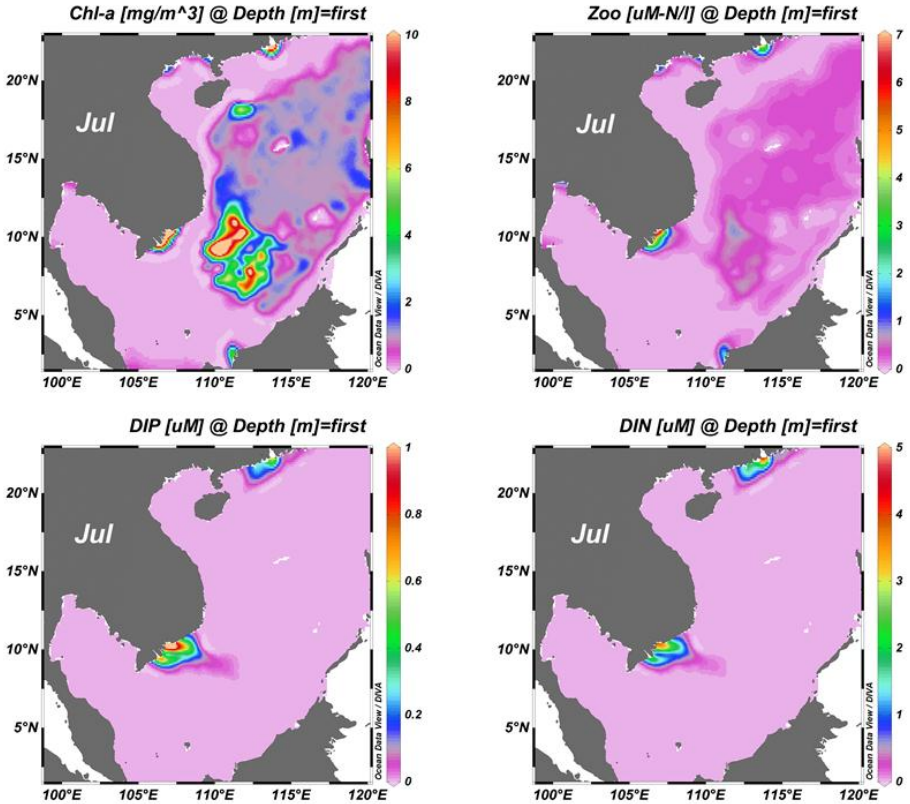

Figure 35. Horizontal distributions of Surface chlorophyll-a, Zooplankton, DIP and DIN during the SWM (July) simulated using POM-NPZD model.

3.2.2. Lower Trophic-Level Ecosystem

Coupled POM-NPZD model is used to calculate the distributions of chlorophyll-a, zooplankton, DIN and DIP in the SCS in the NEM (January) and the SWM (July). The distributions of those parameters seem to follow the courses of circulation passing by the sources of nutrients including the river mouths and the sea boundaries (Figure 34 and 35). Seasonal variations of the courses of nutrients and chlorophyll-a distributions near the Mekong River mouth are discussed as an example for this mention. Nutrients loaded from the Mekong River transport along the coastline to the mouth of the GoT during the NEM and moved to the north during the SWM. These variations are related to seasonal circulation patterns near this area (Figure 31) that direct to the south and the north of the Mekong River mouth during the NEM and SWM, respectively. Nutrient distributions obviously follow these trends. Surface chlorophyll-a however show the same distributions but the distances from the sources seem to be shorter than those of nutrients. It can be explained that the mechanisms of chlorophyll-a or phytoplankton in the ecosystem are very complex. The chlorophyll-a distribution is controlled by many physical, chemical and biological factors (Section 2.2). For example in the upper GoT, the distribution is very sensitive to vertical diffusion or water turbulence (Buranapratheprat et al., 2008). It is not well understood what key mechanisms to control the blooming of plankton in the SCS area really are. Nutrients are admittedly the food source of phytoplankton growth but what physical processes will help to stimulate blooming. Our results suggest that even high nutrients near the river mouths cannot trigger blooming if other physical environments are not appropriate. On the other hand, a strong bloom can develop offshore of the northeast of the Mekong River mouth because of strong upwelling in the area during the SWM (Figure 33). This is an example to support the important of physical processes to stimulate plankton bloom in the SCS. These issues however need to be carefully investigated in the future.

Coupled POM-NPZP model in this study has a limitation in the calculation of chlorophyll-a in the central SCS. Some chlorophyll-a concentrations are observed in the area over the deep basin. This is the effect of Sigma layer used in the model. This kind of grid design adjust the vertical length proportional to the ocean bathymetry. Since SOS basin is very deep (over 5,000 m) and the coastal zone is very shallow (less than 100 m), the size of vertical grids between both areas are very much different. This study used 25 Sigma layers that mean the lengths of vertical grid are about 200 m and less than 4 m for the deep and the shallow areas, respectively. This different has an influent to physical processes and then phytoplankton growth or chlorophyll-a concentration. We are still not exactly know why chlorophyll-a concentration in the deep basin is a little larger than that in the shallow area. The length of Sigma layer in the deep basin (200 m) suggests that calculated chlorophyll-a there may represent the concentration in subsurface instead of surface layers. This effect is very interesting and need to be studied further in the future.

3.2.3. Water Column Analysis

Total dV/dt calculated using Equation 23 reveals that the major peak of estimated stratification occurs in April and May while a minor one occurs in September and October. Surface heat fluxes are the most significant factors to control the variation of water stratifications followed by atmospheric freshwater fluxes. Well-mixing is expected to occur from November to February, observed by negative dV/dt, resulted from relatively large tidal stirring, surface heat loss and low freshwater input. Neutral value (dV/dt ~ 0) is predicted to occur from June to August when all controlling factors are balanced.

Temporal variation of averaged values over the whole gulf area of dV/dt and bottom-surface density difference (delta Sigma-t) is shown in Figure 36 for comparison between the predicted and the real water column conditions. Generally changes in both values are related to each other that high dV/dt occurs when delta Sigma-t is low and vice versa. Negative dV/dt and high delta Sigma-t, and positive dV/dt and low delta Sigma-t correspondingly occurs from April to October and from December to February, respectively. Some discrepancies are found when they are considered in more details. Highest peak of dV/dt (1.16 g s^{-3}) occurs in December but lowest peak of delta Sigma-t (0.4 kg m^{-3}), however, appears in February, two months after the estimated mixing peak. Disagreement between

both values also occurs in summer period. Estimated stratification during June and August dramatically decreases from April and May while delta Sigma-t is still high during the same period. This evidence becomes clear when compared to the situation in March that dV/dt value is almost zero, the same as that during June and August, but delta Sigma-t values are much different, 0.77 kg m^{-3} in March and 1.0 - 1.2 kg m^{-3} during June and August.

Spatial distributions of dV/dt (Figure 37) and delta Sigma-t (Figure 38) are used to investigate more details of the difference between the predicted and the real water column conditions. Water mixing or low delta Sigma-t appears in shallow water surrounding GoT especially in the area near Cape Ca Mau. This is due to strong tidal stirring because tidal amplitude in this area is quite large (0.6 - 0.8 m s^{-1}). The predicted values (Figure 37) show that water mixing in the whole gulf should occur from November to February with the highest peak in December. When compared to delta Sigma-t (Figure 38), some stratification clearly remains during this period and the mixing shifts to February as mentioned previously. Most stratified waters occur in the middle of the GoT and in the southern area outside the GoT where water depths are relatively large. They connect to each other during April and August. Only one area of the stratification in the central GoT is left during December and February.

The prediction results suggest well mixing but the real water condition is stratified in the middle gulf from November to February. Cross sectional salinity contours along central axis in Figure 1 for each month (Figure 39) are used to investigate both water column conditions and interaction between the GoT and the SCS water. The conditions of water mass in the south near east Malaysia, however, seem to follow the dV/dt prediction that well mixing occurs in winter (Figure 38 and Figure 39). Stratification in the central gulf in December comes from low salinity water floating over high salinity water. Freshwater should come from local sources because there is no low salinity connection between inside and outside the GoT (not shown). Remaining large volume of freshwater in the gulf during wintertime is very interesting because local river discharge and precipitation are both small (Figure 3 and Figure 4). This phenomenon may be controlled by oceanographic condition during that time. Since the potential energy of mixing estimated using Equation 1 considered just instantaneous discharge and precipitation, it becomes unable to reproduce stratification due to freshwater buoyancy in such a case.

Resident time of freshwater should be short in summer (the SWM) following enhanced density-driven current and long in winter (the NEM) resulted from inflow water from the SCS. Besides the volume of freshwater inputs, resident time of freshwater play a crucial role to control salinity in the area. Salinity, therefore, should be higher and lower than normal during the SWM and the NEM, respectively. This is used to explain why average salinity in the gulf in dry wintertime is lower than in wet summertime. This explanation agrees very well with the circulation results from this study (Figure 31) that surface current from the SCS flow in and out of the GoT during the NEM and SWM, respectively. Surface water flow into the GoT during the NEM will enhance the resident time of fresh water in the GoT while the surface flow out of the GoT during the SWM will move fresh water out of the GoT faster than normal. This agreement is very useful to explain the seasonal variations in material exchanges between the GoT and the SCS.

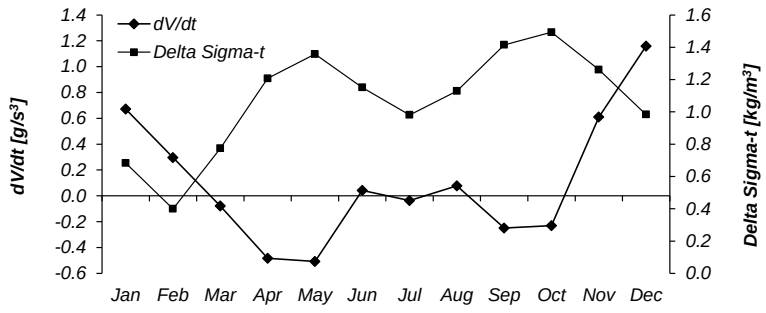

Figure 36. Monthly variations in bottom-surface density difference (Delta Sigma-t) and the rate of change of potential energy (*dV/dt*) in the water column in the Gulf of Thailand.

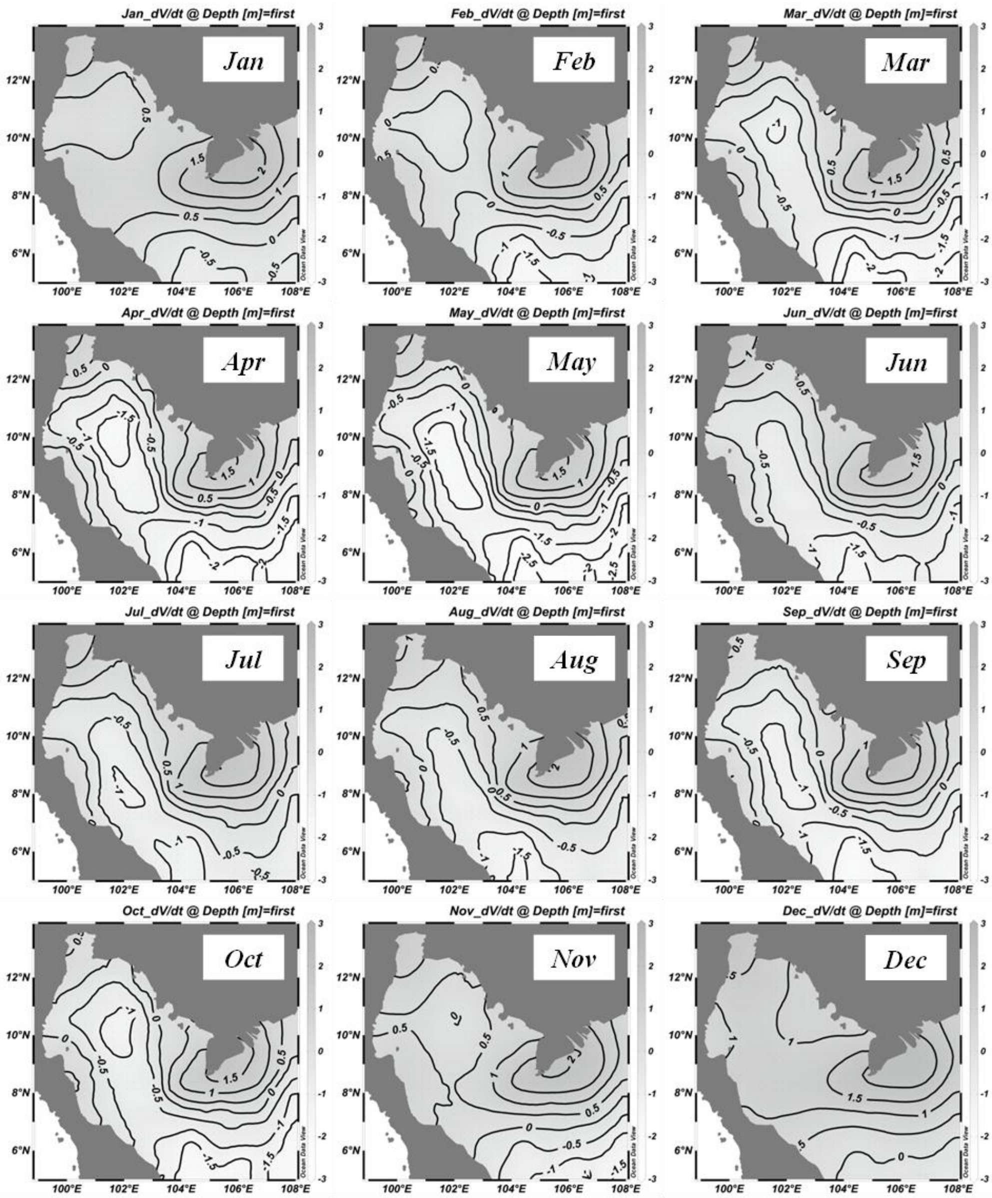

Figure 37. Horizontal distributions of potential energy (*dV/dt*) in the water column (g s^{-3}) for every month.

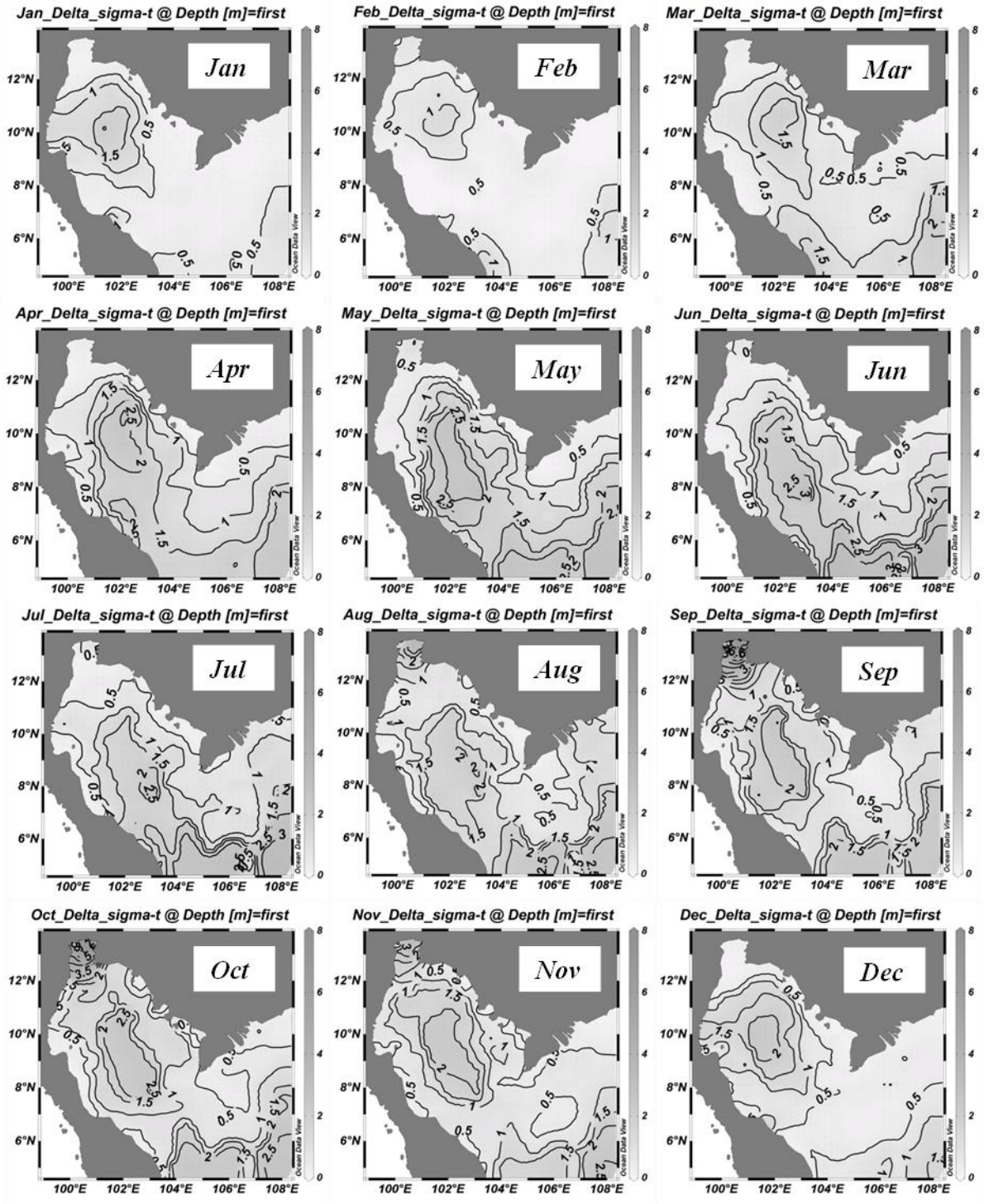

Figure 38. Horizontal distributions of bottom-surface density difference (Delta Sigma-t) (kg m^{-3}) for every month.

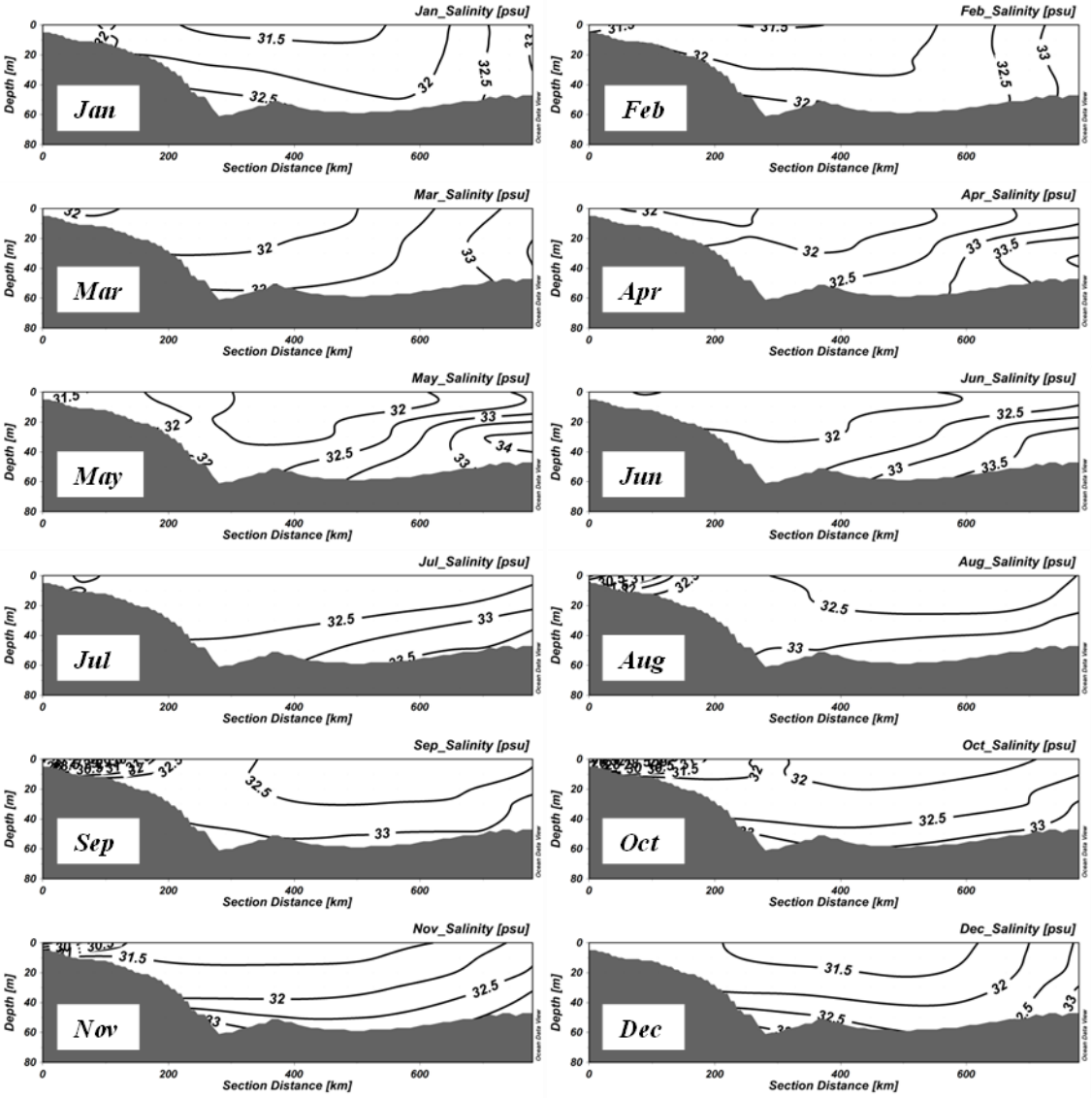

Figure 39. Vertical distributions of climatological salinity along the main axis in the Gulf of Thailand for every month.

Stable strong stratification developed from April to October while dV/dt values suggesting moderate stratification and neutral condition is possibly resulted from the SCS water intrusion into the GoT. The intrusion is expected to occur when the temperature of the GoT water is warmer than that of the SCS in summertime. This density-driven circulation generates surface outward flow, the same direction to Ekman surface current induced by the southwest wind (Yanagi et al., 2001). The subsurface water intrusion from the SCS, therefore, becomes more intense, resulted to strong stratification in the gulf throughout this season. Cross sections of salinity contours near the gulf mouth (Figure 39) clearly animate this dynamics that the intrusion of the SCS starts in April and ends in November.

4. Conclusions

Utilizing multisensory satellite observations and the coupled hydrodynamic-biogeochemical model this research project aims at discerning spatial and temporal variations of phytoplankton Chl-a and/or PP, as well as to identify the probable factors and/or mechanisms underlying the observed Chl-a and/or PP variations in the Asia-Pacific marginal seas. Researches relying on satellite observations were conducted in the marginal seas of the ECS, the SCS, and the SM, whereas researches relying on hydrodynamic-biogeochemical model were conducted in the SCS and the GoT.

The main findings from the multisensor satellite data analysis are described in the followings. The Chl-a in the SM showed seasonal cycle, high (low) during NEM (SWM). There existed however meridional difference in the Chl-a bloom peak timing, earlier in the south, later in the north region of the SM. Wind-driven vertical mixing, wind-driven coastal upwelling, wind-driven Ekman transport, and RD were likely responsible for the observed Chl-a seasonal cycle and variation in the SM. There existed also meridional sensitivity of interannual Chl-a variation in the SM to ENSO and IOD events. The probable drivers for this Chl-a interannual variation associated with climatic anomalies were RD, and atmospheric depositions, both wet (RR) and dry (AOT) depositions. The responsible factors for the observed long-term trend of Chl-a in the SM were still unclear, as none of the investigated environmental variable showed remarkable long-term trend.

In general, seasonal cycle of Chl-a in the SCS resembled that in the SM, i.e., high (low) during NEM (SWM). There existed unique areas showed high Chl-a during summer (winter) in the area west of Vietnam (northwest of Luzon Island). Enhanced summer Chl-a in the area west of Vietnam was caused by southwesterly wind-driven coastal upwelling, whereas enhanced winter Chl-a in the area northwest of Luzon Island was attributed to northeasterly wind-driven upwelling. Chl-a interannual variation in the SCS was responsive to ENSO event. Initially, El Nino decreased Chl-a in the area west of Vietnam, but within 6 months following El Nino signal, Chl-a over the large area in the center of the SCS tended to decline. The declined Chl-a during El Nino event was likely attributed to anomalous anti-cyclonic wind circulation over the SCS.

Unlike in the SM and the SCS, where seasonally high Chl-a was observed during NEM (winter), Chl-a and hence PP in the ECS were high during SWM (summer). High SST and low TSM due to summer calm condition were the main factors allowing summer Chl-a and PP bloom in the ECS. Averaging only within the CDW area, long-term satellite-based PP showed that PP in the area adjacent to the Changjiang estuary had large interannual variation which seems to be attributed to a multitude of factors, such as Changjiang RD, TGD freshwater impoundment, and recent red tide outbreak. The analysis also found that within the last decade, PP in the area adjacent to Changjiang estuary decreased remarkably, though RD and CDW area showed no remarkable trends. TSM indeed showed remarkable decreasing trend, implying that there existed improved water column light quality (due to decreased turbidity) that allowed increasing trend of phytoplankton growth.

The followings are summaries for researches applying numerical and biogeochemical models. Seasonal circulations in the SCS were simulated using POM, a three dimensional ocean model. The results revealed seasonal circulations following the NEM and SWM winds. Strong southward and northward surface flows along Vietnamese coastline developed during the NEM and SWM, respectively. Simulated vertical velocities also revealed upwelling, induced by the southwest wind and surface divergence, in offshore area in the south of Vietnam. POM-NPZD ecosystem model revealed the importance of nutrients supported by rivers to phytoplankton growth. The distributions of surface chlorophyll-a were controlled by complex physical and biochemical mechanisms. Physical conditions including water mixing and stratifications may play some key roles on phytoplankton bloom in the area. Finally, the results of water column analysis for the GoT revealed the influences of the SCS on the GoT water column. Stratification in the GoT seemed to develop year round due to intrusion of the SCS sub-surface water during the SWM and surface flow into the GoT during the NEM. These results agreed well to simulated seasonal circulations using POM in this study.

5. Future Directions

Future directions as a continuation of this research project have been discussed intensively both internal among the collaborators, young scientists involved in this project, as well as among the international participants during the APN-JAMSTEC workshop held in February 2014. Among the future directions are mainly; 1) it has been planned to apply Japan Society for the Promotion of Science (JSPS) Postdoctoral Fellowship for Foreign Researchers with the fellows probably from Vietnam, Malaysia, and China. The host researcher for this JSPS Postdoctoral fellowship is P.I. of this research project; 2) the future research directions will be focused are modeling PP in the SCS and algorithm

developments of Chl-a for MODIS satellite in the ECS and the SM; 3) data sharing was also one of important issues to be addressed. In the future, marine environmental data repository system was strongly recommended for the Asia-Pacific region. In line with this data sharing/management, JAMSTEC under the Group on Earth Observation (GEOS), will again invite scientists (APN-JAMSTEC workshop participants) from Asia-Pacific region to join the Global Earth Observation System of Systems) Symposium to discuss mechanism of meta-data exchange; 4) as a result of post-APN-JAMSTEC workshop, is that another scientific workshop on ocean color satellite application has also been planned with JAMSTEC as organizer.

References

Abram, N.J.; Gagan, M.K.; McCulloch, M.T.; Chappell, J.; Hantoro, W.S. Coral reef death during the 1997 Indian Ocean Dipole linked to Indonesian wildfires. Science 2003, 301, 952–955.

Alvera-Azcarate, A.; Barth, A.; Beckers, J.-M.; Weisberg, R.H. Multivariate reconstruction of missing data in sea surface temperature, chlorophyll, and wind fields. J. Geophys. Res. 2007, 112, C03008, doi:10.1029/2006JC003660.

Amiruddin, A.M.; Ibrahim, Z.Z.; Ismail, S.A. Water mass characteristics in the Strait of Malacca using Ocean Data View. Res. J. Env. Sci. 2011, 5(1), 49–58.

Behrenfeld, M.J.; Falkowski, P.G. Photosynthetic rates derived from satellite-based chlorophyll concentration, Limnol. Oceanogr. 1997, 42, 1–20.

Buranapratheprat, A.; Yanagi, T.; Matsumura, S. Seasonal variation in water column conditions in the upper Gulf of Thailand. Cont. Shelf Res. 2008a, 28, 2509 – 2522.

Buranapratheprat, A.; Yanagi, T.; Niemann, K.O.; Matsumura, S.; Sojisuporn, P. Surface chlorophyll dynamics in the upper Gulf of Thailand revealed by a coupled hydrodynamic-ecosystem model. J. Oceanogr. 2008b, 64, 639 – 656.

Cai, S.; Huang, Q.; Long, X. Three-dimensional numerical model study of the residual current in the South China Sea. Acta Oceanol. 2003, 21, 597 – 607.

Chern, C. S.; Wang, J. Numerical Study of the Upper-Layer Circulation in the South China Sea. J. Oceanogr. 2003, 59, 11 – 24.

Chu, P. C.; Edmons, N. L. A Three-Dimentional Numerical Simulation of the South China Sea Circulation and Thermohaline Structure. Chinese J. Atmos. Sci. 1998, 22(4), 481 – 503.

Di Toro, D.M.; O'Connor, D.J.; Thomann, R.V. 1971. A dynamic model of the phytoplankton population in the Sacramento-San Joaquin Delta, Nonequilibrium systems in natural water chemistry. Adv. Chem. Series, 1971, 106, 131 – 180.

Eppley, R.W. 1972. Temperature and phytoplankton growth in the sea. Fish. Bull. 1972, 70, 1063–1085.

Fang, G. H.; Fang, W. D.; Fang, Y.; Wang K. A survey of studies on the South China Sea upper ocean circulation. Acta Oceanogr. Taiwanica, 1998, 37(1), 1 – 16.

Fang, G.; Kwok, Y. K.; Yu, K.; Zhu, Y. Numerical simulation of principal tidal constituents in the South China Sea, Gulf of Tonkin and Gulf of Thailand. Cont. Shelf Res. 1999, 19, 845 – 869.

Fasham, M.J.R.; Ducklow, H.W.; McKelvie, S.M. A nitrogen-based model of plankton dynamics in the ocean mixed layer. J. Mar. Syst. 1990, 48, 591 – 563.

Gao, J.; Xue, H.; Chai, F.; Shi, M. Modelling the circulation in the Gulf of Tonkin, South China Sea. Ocean Dyn. 2013, 63, 979 – 993.

Gong, G.C.; Liu, G.J. An empirical primary production model for the East China Sea. Cont. Shelf Res. 2003, 23, 213 – 224.

Gong, G.C.; Wen, Y.H.; Wang, B.W.; Liu, G.J. Seasonal variation of chlorophyll a concentration, primary production and environmental condition in the subtropical East China Sea. Deep-Sea Res. II. 2003, 50, 1219 – 1236.

Gong, G.C.; Chang, J.; Chiang, K.P.; Hsiung, T.M.; Hung, C.C.; Duang, S.W.; Codispoti, L.A. Reduction of primary production and changing of nutrient ratio in the East China Sea: effect of the Three Gorges Dam? Geophys. Res. Lett. 2006, 33(7).

Gordon, H.R.; Wang, M. Retrieval of water-leaving radiance and aerosol optical thickness over the oceans with SeaWiFS: a preliminary algorithm. Appl. Opt. 1994, 33, 443–452.

Guo, X.; Yanagi, T. The role of Taiwan Strait in an ecological model in the East China Sea. Acta Ocean. Taiwanica, 1998, 37 (2), 139 – 164.

Hu, J.; Kawamura, H.; Hong, H.; Qi, Y. A Review on the Currents in the South China Sea: Seasonal Circulation, South China Sea Warm Current and Kuroshio Intrusion. J. Oceanogr. 2000, 56, 607 – 624.

Huot, Y.; Babin, M.; Bruyant, F.; Grob, C.; Twardowski, M.S.; Claustre, H. Does chlorophyll a provide the best index of phytoplankton biomass for primary production studies? Biogeosci. Disc. 2007, 4, 707 – 745.

Ibrahim, Z.Z.; Yanagi, T. The influence of the Andaman sea and the South China sea on water mass in the Malacca Strait. Mer. 2006, 43, 33–42.

Iverson, R.L. Control of marine fish production. Limnol. Oceanogr. 1990, 35(7), 1593 – 1604.

Kawamiya, M.; Kishi, M.J.; Yamanaka, Y.; Suginohara N. An ecological-physical coupled model applied to Station Papa. J. Oceanogr. 1995, 51, 635 – 664.

Li, L.; SongHui, L.; Tao, J.; Xia, L. Seasonal variation of size-fractionated phytoplankton in the Pearl River estuary. Chinese Sci. Bull. 2013, 58, 2303 – 2314.

Liu, S.M.; Hong, G.-H.; Zhang, J.; Ye, X. W.; Jiang, X. L. Nutrient budgets for large Chinese estuaries. Biogeosciences 2009, 6, 2245 – 2263.

Liu, K.K.; Chao, S.Y.; Lee, H.J.; Gong, G.C.; Teng, Y.C. Seasonal variation of primary productivity in the East China Sea: A numerical study based on coupled physical-biogeochemical model. Deep-Sea Res. II. 2010, 57, 1762 – 1782.

Luadnakrob, P.; Buranaprattheprat, A. Annual surface heat flux in the Gulf of Thailand. Burapha Sci. 2012, 17 (1), 77 – 86 (in Thai with English abstract).

Mellor, G.L. User's Guide for a Three-Dimensional, Primitive Equation, Numerical Ocean Model. Program in Atmospheric and Oceanographic Sciences Report 1998, Princeton University, Princeton, N.J.; 41 pp.

Mekong River Commission. The Flow of the Mekong. MRC Management Information booklet series 2009, No. 2, 12 pp.

Morimoto, A.; Yoshimoto, K.; Yanagi, T. Characteristics of Sea Surface Circulation and Eddy Field in the South China Sea Revealed by Satellite Altimetric Data. J. Oceanogr. 2000, 56, 331 – 344.

Naik, H.; Chen, C.-T. A. Biogeochemical cycling in the Taiwan Strait. Estuarine, Coastal and Shelf Science 2008, 78, 603 – 612.

Nybakken, J.W.; Bertness, M.D. Marine Biology: An Ecological Approach (6th ed.). 2004, Benjamin Cummings, CA, 592 pp.

O'Connor, D.J.; Di Toto, D.M.; Thomann R.V. Phytoplankton models and eutrophication problems. In Ecological Modeling in a Resource Management Framework ed. C.S. 1975, Russell, Resources for the Future, Washington DC.

O'Reilly, J.E.; Maritorena, S.; Mitchell, B.G.; Siegel, D.A.; Carder, K.L.; Garver, S.A.; Kahru, M.; McClain, C.R. Ocean color chlorophyll algorithms for SeaWiFS. J. Geophys. Res. 1998, 103(C11), 24937–24953.

Onitsuka, G.; Yanagi, T. Differences in ecosystem dynamics between the northern and southern parts of the Japan Sea: Analyses with two ecosystem models. J. Oceanogr. 2005, 61, 415 – 433.

Onitsuka, G.; Yanagi, T.; Yoon, J-H. A numerical study on nutrient sources in the surface layer of the Japan Sea using a coupled physical-ecosystem model. J. Geophys. Res. 2007, 112, C05042, doi:10.1029/2006JC003981.

Parsons, T.R.; Takahashi, M.; Hargrave, B. Biological Oceanographic Processes 1984, (3rd ed.), Pergamon, 330 pp.

Riley, G.A. Oceanography of Long Island Sound, 1952-1954, II. Phys. Oceanogr. Bull. Bing. Ocean. Coll. 1956, 15, 15 – 46.

Robinson, M. K. The physical oceanography of the Gulf of Thailand, Naga Expedition. In: NAGA Report Volume 3: Scientific Results of Marine Investigations of the South China Sea and the Gulf of Thailand 1959-1961. The University of California, 1974, Scripps Institution of Oceanography, La Jolla, California.

Ryther, J. H. Photosynthesis and fish production in the sea. Science 1969, 166(3901), 72 – 76.

Shang, S.; Li, L.; Li, J.; Li, Y.; Lin, G.; Sun, J. Phytoplankton bloom during the northeast monsoon in the Luzon Strait bordering the Kuroshio. Rem. Sens. Env. 2012, 124, 38 – 48.

Simpson, J.H.; Bowers, D. Models of stratification and frontal movement in shelf seas. Deep-Sea Res., 1981, 28A (7), 727 – 738.

Siswanto, E.; Ishizaka, J.; Yokouchi, K. Optimal primary production model and parameterization in the eastern East China Sea. J. Oceanogr. 2006, 62, 361 – 372.

Siswanto, E.; Nakata, H.; Matsuoka, Y.; Tanaka, K.; Kiyomoto, Y.; Okamura, K.; Zhu, J.; Ishiaka, J. The long-term freshening and nutrient increases in summer surface water in the northern East China Sea in relation to Changjiang discharge variation. J. Geophys. Res. 2008, 113 (C10030).

Siswanto, E.; Tang, J.; Yamaguchi, H.; Ahn, Y.H.; Ishizaka, J.; Yoo, S.; Kim, S.W.; Kiyomoto, Y.; Yamada, K.; Chiang, C.; Kawamura, H. Empirical ocean-color algorithm to retrieve chlorophyll-a, total suspended matter, and colored dissolved organic matter absorption coefficient in the Yellow and East China Seas. J. Oceaogr. 2011, 67(5), 627–650.

Siswanto, E.; Tanaka, K. Phytoplankton biomass dynamics in the Strait of Malacca within the period of the SeaWiFS full mission: seasonal cycles, interannual variations, and decadal-scale trends. Rem. Sens. (in press).

Smayda, T.J. The suspension and sinking of phytoplankton in the sea. Mar. Biol. Ann. Rev. 1970, 8, 353 – 414.

Smayda, T.J. 1973. The growth of Sceletonema costatum during a winter-spring bloom in Narragansett Bay. Norwegian J. Bot. 1973, 20, 219 – 247.

Snidvongs, A. The oceanography of the Gulf of Thailand: Research and management policy 1998, pp 1 – 68. In: D. M. Johnston (ed.) SEAPOL Integrated Studies of the Gulf of Thailand, Vol. 1. Southeast Asian Programme in Ocean Law, Policy and Management.

Stansfield, K.; Garrett, C. Implications of the salt and heat budgets of the Gulf of Thailand. J. Mar. Res. 1997, 55, 935 – 963.

Staub, J. R.; Among, H. L.; Gastaldo, R. A. Seasonal sediment transport and deposition in the Rajang River delta, Sarawak, East Malaysia. Sed. Geolog. 2000, 133, 249 – 264.

Stewart, R.H. Introduction to Physical Oceanography. Texas A & M University, 2006, 344 pp. http://oceanworld.tamu.edu/resources/ocng_textbook/PDF_files/book_pdf_files.html.

Tan, C.K.; Ishizaka, J.; Matsumura, S.; Yusoff, F.Md.; Mohamed, M.I., 2006. Seasonal variability of SeaWiFS chlorophyll a in the Malacca Straits in relation to Asian monsoon. Cont. Shelf Res. 2006, 26, 168 – 178.

Tang, D.; Kawamura, H.; Lee, M.A.; Dien, T.V. Seasonal and spatial distribution of chlorophyll-a concentration and water condition in the Gulf of Tonkin, South China Sea. Rem. Sens. Envi. 2003, 85(4), 475 – 483.

Tang, D. L.; Kawamura, H.; Shi, P.; Takahashi, W.; Guan, L.; Shimada, T.; Sakaida, F.; Isoguchi, O. Seasonal phytoplankton blooms associated with monsoonal influences and coastal environments in the sea areas either side of the Indochina Peninsula. Geophys. Res. 2006, 111, G01010, doi:10.1029/2005JG000050.

Wang, Y.; Field, R.D.; Roswintiarti, O. Trends in atmospheric haze induced by peat fires in Sumatra Island, Indonesia and El Niño phenomenon from 1973 to 2003. Geophys. Res. Lett. 2004, 31, L04103, doi:10.1029/2003GL018853.

Wosten, J. H. M.; Willigen, P. de.; Tri, N. H.; Lien, T.V.; Smith, S.V. Nutrient dynamics in mangrove areas of the Red River Estuary in Vietnam. Estuarine. Coast. Shelf Sci. 2003, 57, 65 – 72.

Wyrtki, K. Physical oceanography of Southeast Asian waters 2. Scripps Institution of Oceanography, La Jolla, CA., 1961, p. 195.

Wyrtki, K. Scientific results of marine investigations of the South China Sea and the Gulf of Thailand. Naga Report 2, 1961, 195 pp.

Yamagata, T.; Behera, S. K.; Luo, J.-J.; Masson, S.; Jury, M. R.; Rao, S. A. Coupled Ocean-Atmosphere Variability in the Tropical Indian Ocean, in Earth's Climate (eds C. Wang, S.P. Xie and J.A. Carton), 2013, American Geophysical Union, Washington, D. C. doi: 10.1029/147GM12.

Yanagi, T. Coastal Oceanography. Terra Scientific Publishing Company, 1999, Tokyo, 162 pp.

Yanagi, T.; Mizuno, Y.; Hoshika, A.; Tanimoto , T. Vertical flow and sinking velocities of particles estimated by a box model in Osaka Bay. Bull. Coast. Oceanogr. 1993, 31, 121 – 128 (in Japanese with English abstract).

Yanagi, T.; Sachoemar, S.I.; Takao, T.; Fujiwara, S. Seasonal variation of stratification in the Gulf of Thailand. J. Oceanogr. 2001, 57, 461 – 470.

Yanagi, T.; Takao, T. A numerical simulation of tides and tidal currents in the South China Sea. Acta Oceanogr. Taiwanica 1998, 37, 17 – 29.

Yelland, M.; Taylor, P.K. Wind stress measurements from the open ocean. American Meteor. Soc. 1996, 26, 541 – 558.

Yuan, J.; Hayden, L.; Dagg, M. Comment on "Reduction of primary production and changing of nutrient ratio in the East China Sea: Effect of the Three Gorges Dam?" Geophys. Res. Lett. 2007, 34, L14609.

Zhang, J.; Gilbert, D.; Gooday, A.J.; Levin, L.; Naqvi, S.W.A.; Middelburg, J.J.; Scranton, M.; Ekau, W.; Pena, A.; Dewitte, B.; Oguz, T.; Monteiro, P.M.S.; Urban, E.; Rabalais, N.N.; Ittekkot, V.; Kemp, W.M.; Ulloa, O.; Elmgren, R.; Escobar-Briones, E.; Van der Plas, A.K. Natural and human-induced hypoxia and consequences for coastal areas: synthesis and future development. Biogeosciences 2010, 7, 1443 –1467.

Zhao, H.; Tang, D.L. Effect of 1998 El Niño on the distribution of phytoplankton in the South China Sea. J. Geophys. Res. 2007, 112, C02017, doi:10.1029/ 2006JC003536.

Appendix (in separated file)